Spherical Spindle Shape Promotes Perpendicular Cortical Orientation by Preventing Isometric Cortical Pulling on both Spindle Poles during *C. elegans* Female Meiosis

Elizabeth Vargas[1,3], Karen P. McNally[1,3], Daniel B. Cortes[2], Michelle T. Panzica[1], Brennan Danlasky[1], Qianyan Li[1], Amy Shaub Maddox[2] and Francis J. McNally[1,4]

1. Department of Molecular and Cellular Biology

   University of California, Davis

   Davis, CA 95616

2. Biology Department

   University of North Carolina

   Chapel Hill, NC 27599

3. Contributed equally to this work

4. Corresponding author

Abstract

Meiotic spindles are positioned perpendicular to the oocyte cortex to facilitate segregation of chromosomes into a large egg and a tiny polar body. In *C. elegans*, spindles are initially ellipsoid and parallel to the cortex before shortening to a near spherical shape with flattened poles and then rotating to the perpendicular orientation by dynein-driven cortical pulling. The mechanistic connection between spindle shape and rotation has remained elusive. Here we used three different genetic backgrounds to manipulate spindle shape without eliminating dynein-dependent movement or dynein localization. Ellipsoid spindles with flattened or pointed poles became trapped in either a diagonal or a parallel orientation. Mathematical models that recapitulated the shape dependence of rotation indicated that the lower viscous drag experienced by spherical spindles prevented recapture of the cortex by astral microtubules emanating from the pole pivoting away from the cortex. In addition, maximizing contact between pole dynein and cortical dynein stabilizes flattened poles in a perpendicular orientation and spindle rigidity prevents spindle bending that can lock both poles at the cortex. Spindle shape can thus promote perpendicular orientation by three distinct mechanisms.

Introduction

The vast majority of eukaryotes are diploid and reproduce sexually using the conserved process of meiosis. Oocytes of most animals undergo a highly asymmetric meiosis in which only one of four sets of maternal chromosomes is inherited by a zygote. Female meiotic spindles are positioned with one pole closely apposed to the oocyte cortex during anaphase. This perpendicular orientation of the meiotic spindle facilitates asymmetric cell divisions that deposit half the homologous

chromosomes in a first polar body and half the remaining sister chromatids in a second polar body (Fabritius et al., 2011a).

In *C. elegans*, the precursor of the meiotic spindle, the germinal vesicle, migrates from the center of the oocyte to the cortex through a mechanism that requires kinesin-1 heavy chain (UNC-116) and its binding partner KCA-1 (Yang et al., 2005; McNally et al., 2010). At nuclear envelope breakdown, the spindle assembles near the cortex, then migrates an average of 2 μm towards the cortex and adopts a roughly parallel orientation to it. The spindle maintains this parallel orientation and an ellipsoid spindle shape (axial ratio 1.3) with a steady state length of 8 μm, for an average of 7 minutes. Then, in a stereotypical series of anaphase promoting complex (APC)-dependent events (Yang et al., 2003; Yang et al., 2005), the spindle shortens in the pole-to-pole axis, achieving an axial ratio 1.0, then rotates to a perpendicular orientation with one pole moving closer to the cortex (Crowder et al., 2015). Anaphase A chromosome separation initiates during or just after rotation as the spindle continues to shorten to an axial ratio of 0.8. Upon completion of anaphase A, the perpendicular spindle elongates and transforms into a cylindrical shape as anaphase B progresses. Finally, the half spindle proximal to the cortex is pushed through the cytokinetic ring (Dorn et al. 2010) or the cytokinetic ring ingresses to the spindle midpoint (Fabritius et al., 2011b) and the chromosomes at the cortex are partitioned into a polar body.

In embryos depleted of either kinesin-1 (UNC-116) or its binding partner, KCA-1, nuclear migration and early translocation of the spindle to the cortex fail, resulting in metaphase spindles that are, on average, 7 μm from the cortex (McNally et al., 2010; Yang et al., 2005). However, upon APC activation, as the spindle begins to shorten, it translocates to the cortex. This compensatory late translocation

in kinesin-depleted embryos occurs at the same time and appears to occur by the same mechanism as spindle rotation in control embryos because both movements require the anaphase promoting complex (Yang et al., 2005), cyclin-dependent kinase (CDK1) inactivation (Ellefson and McNally, 2011) and cytoplasmic dynein (van der Voet et al., 2009; Ellefson and McNally, 2009). Initiation of dynein-dependent spindle rotation correlates with spherical spindle shape even when spindle shape is manipulated by changing ploidy (Crowder et al., 2015) but the mechanistic reason for the correlation between shape and orientation has remained obscure.

Well characterized dynein-dependent spindle positioning mechanisms involve astral microtubules with minus ends attached to a centrosome or spindle pole body and plus ends that interact with cytoplasmic dynein anchored at the cell cortex (McNally, 2013; Kotak, 2019). The mechanism of dynein-dependent meiotic spindle positioning is less understood. *C. elegans* meiotic spindles, like those of mammals (Szollosi et al., 1972; Sathananthan, 1985), have no centrosomes (Albertson and Thomson, 1993). Although *C. elegans* meiotic spindles have astral microtubules and cortical dynein (Crowder et al., 2015), it is unclear how the minus ends of astral microtubules would be anchored in an acentrosomal spindle pole to allow pulling by cortical dynein. *C. elegans* meiotic embryos also have cortical microtubules and these microtubules are inferred to have minus ends anchored at the cortex and plus ends oriented inward because they allow kinesin-1 (UNC-116) dependent packing of yolk granules into the embryo interior (McNally et al., 2010; Kimura et al., 2017). Plus ends of the cortical microtubules might interact with dynein that accumulates on spindle poles during rotation (Ellefson and McNally, 2011). However, it is unclear how dynein could be anchored at an acentrosomal spindle pole in a manner that

would allow pulling on the plus ends of cortical microtubules. Recently, Tan et al. (2018) demonstrated that when a threshold number of dynein, dynactin, BicD2N complexes accumulate at a microtubule minus end, they acquire the ability to capture a second microtubule and move the minus end of the first microtubule toward the minus end of the second microtubule. This mechanism could explain how spindle pole dynein could pull on the plus ends of cortical microtubules or how the minus ends of astral microtubules would be mechanically attached to the spindle when pulled by cortical dynein. Meiotic spindle rotation requires ASPM-1, LIN-5, dynein and dynactin (van der Voet et al., 2010; Crowder et al., 2015) and it is possible that ASPM-1/LIN-5 substitutes for BicD2N during spindle rotation to generate cortical pulling on spindle poles.

To test whether spherical spindle shape is required for spindle rotation, we sought genetic backgrounds with more elongated spindles. Depletion of dynein, dynactin, LIN-5 or ASPM-1 results in long spindles (Ellefson and McNally, 2011; Connolly et al., 2014; Crowder et al., 2015), however, these proteins are implicated in dynein-dependent force generation that is also required for spindle rotation. Katanin is a microtubule-severing protein composed of two subunits encoded by the *mei-1* and *mei-2* genes in *C. elegans*. While, strong loss-of-function katanin mutants assemble meiotic spindles with no ASPM-1 labelled spindle poles (McNally and McNally, 2011; Connolly et al., 2014), the partial loss-of-function mutant, *mei-2(ct98)*, which has reduced microtubule-severing activity (McNally et al., 2014), assembles elongated bipolar spindles with rotation defects (McNally et al., 2006). In this study, we identified a transgene that restores both short length and spindle rotation to katanin mutant spindles. We also found that double depletion of two kinetochore proteins, KNL-1 and KNL-3, resulted in long spindles and a rotation defect. Thus,

lengthening spindles via the use of two unrelated genetic manipulations prevented rotation and suppressing the length defect of one mutant restored rotation. Our results suggest that elongated spindles fail to rotate because of their shape rather than a failure of cortical pulling.

Results

mei-2(ct98) spindles and knl-1,3(kd) spindles frequently fail to rotate.

Whereas 100% (n=22) of control meiotic spindles rotated to a stable perpendicular orientation (80-90° to the tangent of the curve of the cortex) (Fig. 1A), 85% (n=27) of *mei-2(ct98)* spindles failed to rotate to the perpendicular orientation. In some cases (14/27 embryos), the *mei-2(ct98)* spindle started to rotate but stalled at a shallow angle (15-80° to the tangent of the curve of the cortex) with one pole touching the cortex (Fig. 1B). In more extreme cases (9/27 embryos), *mei-2(ct98)* spindles did not rotate and anaphase proceeded on spindles that had both poles near the cortex (0-15°; Fig. 1C). Two polar bodies frequently started to form over both separated masses of chromosomes on these completely parallel spindles but then regressed. The frequency of completely parallel anaphases corresponds with embryonic lethality in this strain (24.2% n= 347; Fisher's exact test p = .35). Because there is some subjectivity in measuring the angle of a spindle relative to an irregular ellipsoid surface, we sought a more objective criterion for correct rotation. *C. elegans* meiotic spindles have 6 regularly spaced bivalents so that 3 - 4 bivalents are visible in a mid-focal plane. In 38/40 control spindles, 3 or more homologous chromosomes merged with the cortex during anaphase (Fig. 1A, 1:45). In contrast, in the majority (30/40) of *mei-2(ct98)* spindles, fewer than 3 homologous chromosomes merged with the cortex (Fig. 1B, 1:45).

Because *mei-2(ct98)* might affect parameters other than spindle shape, we sought a means to alter spindle shape by a different mechanism. Because increased chromosome number results in increased spindle width (Crowder et al., 2015), we hypothesized that a defect in chromosome congression might lead to decreased spindle width. To induce a congression defect, we double depleted the kinetochore proteins, KNL-1 and KNL-3, either by GFP(RNAi) of endogenously GFP-tagged genes or with auxin-inducible degrons (see Methods). We found that in a subset of embryos depleted of KNL-1 and KNL-3, referred to as *knl-1,3(kd)* (kd = knock down), spindles were indeed narrower (see below), possibly because chromosomes are stacked end to end rather than side by side (Fig. 1D). 5/25 *knl-1,3(kd)* spindles underwent partial rotation (15-80°) and 5/25 *knl-1,3(kd)* spindles completely failed to rotate (0-15°) and underwent parallel anaphase (Fig. 1D).

Because spindle shortening and rotation are driven by cyclin-dependent kinase (CDK-1) inactivation (Ellefson and McNally, 2011), defects in rotation might be caused by disruptions in cell cycle timing. However, the time from the initiation of spindle shortening to the initiation of cortical invaginations that mediate polar body formation was not significantly different between control and *mei-2(ct98)* time-lapse sequences (control: mean 334 sec ± 15 sec SEM n= 12; *mei-2(ct98)*: mean 341 sec ± 14 sec n=14, p = 0.73 Student's t test) or between control and *knl-1,3(kd)* time-lapse sequences (control: mean 362 sec ± 80 sec SEM n= 16; *knl-1,3(kd)*: mean 351 sec ± 24 sec n=10, p = 0.74 Student's t test).

Spindles with elongated shapes fail to rotate to 90°.

We previously reported a correlation between wild-type spindle rotation and an axial ratio of 1.0 at the time of rotation (Crowder et al., 2015). If this short axial ratio is required for spindle rotation, then spindles with higher axial ratios should fail to rotate. We previously found that p150 dynactin (DNC-1)-depleted metaphase spindles had elongated axial ratios and shortened to variable extents. The subset of DNC-1-depleted spindles that shortened to an axial ratio of 1.0 by anaphase onset still failed to rotate, indicating a role in cortical pulling independent of a role in spindle shape (Crowder et al., 2015). Both *mei-2(ct98)* and *knl-1,3(kd)* spindles also underwent shortening to variable extents. Because wild-type rotation initiates roughly 15 sec before anaphase onset, we determined the axial ratio 15 sec before anaphase onset to allow comparison of spindles that rotated to a perpendicular orientation with those that partially rotated to a diagonal orientation and with those that did not rotate, resulting in parallel anaphase. At this timepoint, average axial ratios of *mei-2(ct98)* spindles that partially rotated or failed to rotate were significantly greater than those of control spindles or *mei-2(ct98)* spindles that did rotate (Fig. 2A). Four long spindles did rotate completely. This could be explained by a strong threshold effect at an axial ratio just under 1.5 (Fig. 2A, 2B). An alternative explanation is that these long spindles that rotated were already oriented at steep angles (>60°) and rotated further toward 90° whereas long *mei-2(ct98)* spindles that started at shallow angles either maintained the parallel orientation or became more parallel (Fig. 2C). The axial ratio of *knl-1,3(kd)* spindles that partially rotated or did not rotate was also significantly higher than that of those spindles that did rotate (Fig. 2B). Thus two unrelated genetic manipulations, *mei-2(ct98)* and *knl-1,3(kd)*, that

caused high axial ratios at the time of normal rotation also caused rotation failure specifically in the subset of spindles with long axial ratios.

In addition to large axial ratios, *mei-2(ct98)* spindles had poles that remained pointed in shape throughout metaphase and anaphase (Fig. 1B; Fig. 2D), whereas control spindle poles became round as rotation started and became partially flattened during rotation so that the curve of the pole closely matched the curve of the cortex (Fig. 1A; 2D). If the width of the LIN-5 measured 0.5 μm from the tip of the spindle is used to calculate the potential surface area of contact between LIN-5 on the pole and LIN-5 on the cortex after rotation to a perpendicular orientation, control spindles would have an average of 8.5 μm^2 of contact whereas *mei-2(ct98)* spindles would only have 1.3 μm^2 of contact. The pointed *mei-2(ct98)* spindle poles would clearly maximize the surface area of contact between pole LIN-5 and cortical LIN-5 when one spindle pole is apposed to the cortex at a shallow angle (Fig. 1B). In contrast with *mei-2(ct98)* spindles, *knl-1,3(kd)* spindles that had long axial ratios had flatter poles (Fig. 2D) more similar to controls, indicating that long axial ratios can interfere with rotation independently of pointed poles.

Unexpectedly, we found that an mKate2 fusion to the PIP2-binding plekstrin homology domain of rat phospholipase C delta (henceforth referred to as mKate::PH) significantly (p= 0.0001 Fisher's exact test) reduced embryonic lethality of *mei-2(ct98)* at 25°C from 24% (n=347) to 14% (n=700). mKate::PH localized only to the plasma membrane (Fig. 3A) and did not affect viability or rotation of control spindles (not shown and Fig. 3A). Early in meiosis, *mei-2(ct98)* + mKate::PH spindles had high axial ratios and pointed poles (Fig. 3B, C) similar to those of *mei-2(ct98)* spindles (Fig. 1B). Like the majority of *mei-2(ct98)* spindles (Fig. 1B), *mei-2(ct98)* + mKate::PH spindles partially rotated to a diagonal orientation (Fig. 1B, 7

min). After achieving close cortical contact in this diagonal orientation, the spindles shortened and poles flattened as they rotated (Fig. 3B, D). 12/13 *mei-2(ct98)* + mKate::PH spindles eventually rotated to 60° or greater (Fig. 3B, 9:45). This contrasts with *mei-2(ct98)* spindles without mKate::PH which did not shorten after cortical contact and did not rotate to 60° or greater (Fig. 1B, 3D). Thus a transgene that caused *mei-2(ct98)* spindles to shorten after cortical contact also caused these spindles to rotate further. This result further supports a direct role for short axial ratios in spindle rotation.

Both *mei-2(ct98)* and *knl-1,3(kd)* spindles exhibit chromosome congression defects (Fig. 1C, D; Dumont et al., 2010) raising the possibility that chromosome congression defects cause rotation defects. However, *knl-1,3(kd)* spindles with near wild-type axial ratios rotated normally (Fig. 2B) even though 11/15 of these spindles had congression defects. Thus congression defects are not sufficient to cause rotation failure. 10/10 *knl-1,3(kd)* spindles with elongated axial ratios had congression defects. Thus it is possible, as suggested above, that a specific arrangement of misaligned chromosomes, end to end stacking, causes spindles to be narrower.

Dynein-dependent movement of spindle poles toward the cortex occurs in *mei-2(ct98)* embryos.

mei-2(ct98) rotation failure could be due to defective dynein-dependent cortical pulling rather than altered spindle shape. In embryos depleted of kinesin-1 (UNC-116) or its binding partner, KCA-1, late translocation of the spindle to the cortex is dynein-dependent (van der Voet et al., 2009; Ellefson and McNally, 2009). To test whether *mei-2(ct98)* embryos are defective in dynein-dependent spindle

movement, we compared the velocities of late spindle translocation in 18 time-lapse sequences of *kca-1(RNAi)* embryos with those in 18 time-lapse sequences of *mei-2(ct98); kca-1(RNAi)* double mutant embryos. Whereas velocities could be determined from all of these sequences, spindle orientation could only be unambiguously scored in a subset, either because of the angle relative to the imaging plane or due to spherical aberration for deeper spindles. In embryos depleted of KCA-1, metaphase spindles are far from the cortex until spindle shortening initiates. As spindles shorten, they move toward the cortex in an APC-(Yang et al., 2005) and dynein-dependent (Ellefson and McNally, 2009) manner (Fig. 4A). In the majority of *kca-1(RNAi)* time-lapse sequences (12/13), this movement was initially a sideways "late translocation" followed by rotation to a perpendicular orientation at the cortex.   *kca-1(RNAi)* spindles underwent late translocation at 2.83 ± .30 μm/min (n=18) (Fig. 4B, D) and *mei-2(ct98); kca-1(RNAi)* double mutant spindles underwent late translocation (15/16 sideways) at 2.67 ± .18 μm/min (n=18) (Fig. 4C, D). Of the *mei-2(ct98); kca-1(RNAi)* spindles which translocated, 6/12 also rotated upon reaching the cortex, while 6/12 remained in a parallel orientation to the cortex during anaphase. The sideways spindle orientation and identical late translocation velocities between *kca-1(RNAi)* and *mei-2(ct98); kca-1(RNAi)* suggested that dynein-dependent cortical pulling is acting on both spindle poles and that any differences in viscous drag on long vs short spindles are insignificant relative to pulling by multiple dynein motors. In addition, these results indicated that rotation failure in *mei-2(ct98)* embryos is not due to a lack of dynein-dependent cortical pulling.

Dynein and dynein regulators localize to the cortex and spindle poles in *mei-2(ct98)* and *knl-1,3(kd)* embryos.

If the altered shape of *mei-2(ct98)* and *knl-1,3(kd)* spindles leads to rotation failure because dynein engages in cortical pulling on both poles, then the dynamic localization of dynein and its regulators should be the same as in controls. In 11/11 control (Fig. 5A) and 18/18 *mei-2(ct98)* embryos (Fig. 5B), the amount of the dynein regulator, DNC-2, increased at the cortex during APC-activated spindle shortening. In both control and *mei-2(ct98)* embryos, the fluorescence intensity of cortical GFP::DNC-2 increased significantly between -90 seconds before initial contact of a pole with the cortex and +90 seconds after initial contact of the pole with the cortex (Fig. 5G). Likewise, the concentration of endogenously tagged dynein heavy chain, DHC-1, increased at the embryo cortex after close contact of the pole with the cortex in both control (Fig. 5C,G) and *knl-1,3(kd)* embryos (Fig. 5D,G). GFP::DNC-2 was present on the poles of control and *mei-2(ct98)* spindles (Fig. 5A,B arrows; Fig. S2 A-D) and mNeonGreen::DHC-1 was present on the poles of control and *knl-1,3(kd)* spindles (Fig. 5C, D arrows; Fig. S2 E-F). Dynein (Fig. 5C,D), dynactin (Fig. 5A,B) and the dynein regulator LIN-5 (Fig. 5E,F) on spindle poles appeared to merge with the cortical pools of these proteins as cortical fluorescence intensity increased. A spindle pole was never observed to dissociate from the cortex after this merging between pole and cortical dynein/dynactin/LIN-5 occurred. These results indicated that *mei-2(ct98)* embryos and *knl-1,3(kd)* embryos have normal levels of dynein-dependent cortical force generators. This result is consistent with a model in which both poles frequently engage in cortical pulling.

Modeling reveals that spherical spindle shape reduces the probability of isometric cortical pulling on both spindle poles.

To separate the possible role of spindle shape from other factors, like microtubule dynamic instability parameters, that might change with any genetic manipulation, we generated mathematical models of rotation using Cytosim (Nedelec and Foethke, 2007), an easily customizable simulation of mixtures of cytoskeletal filaments and motor proteins. In these two-dimensional simulations, spindles of 4 different shapes were built as solid objects with astral microtubules extending from nucleators at the spindle poles. "Short flat" spindles had aspect ratios of 0.9 and slightly flattened poles to mimic the shape of wild-type spindles mid-rotation. "Long pointed" spindles had aspect ratios of 1.5 and pointed poles to mimic the shape of *mei-2(ct98)* spindles that partially rotated. To distinguish between the relative importance of axial ratio vs flattened poles, "long flat" spindles similar to *knl-1,3(kd)* spindles, and imaginary "short pointed" spindles were also built. Astral microtubules emanated from nucleators arranged to mimic the localization of LIN-5/dynein in wild-type, *knl-1,3(kd)* or *mei-2(ct98)* spindle poles and astral microtubules underwent dynamic instability. Starting with *in vivo* dynamic instability parameters taken from Kline-Smith and Walczak (2002), a limited parameter sweep was conducted to find conditions that allowed short flat spindles to rotate within 300 seconds, the normal time between initiation of spindle shortening, indicative of APC activation, and completion of anaphase A. Short 200 nm cortical microtubules emanated from nucleators at the cortex (green dots in Fig. 6A). Dynein complexes (red dots) in the cytoplasm bound to astral or cortical microtubules, motored toward minus ends and dissociated with a rate constant that increased with applied force. When a dynein complex contacted an astral microtubule and a cortical microtubule, the spindle was

transiently pulled toward the cortex. A stabilizing "cortical glue" (purple dots) was included so that spindles became more stably attached once close contact between the pole and the cortex was achieved. This cortical glue was intended to mimic the increased concentration of cortical dynein after pole contact (Fig. 5). Excluding this cortical glue had no significant impact on the results (see Methods). Spindles were initially perfectly parallel to and 2 μm away from the cortex at the start of each simulation, and simulations were run for 300 seconds. In nearly all cases, spindles initially moved toward the cortex in a sideways orientation and astral microtubules from both poles made pulling contacts with cortical microtubules for durations ranging from 3 – 248 seconds (Movies 1-8). The initial sideways movement of simulated spindles matched the initial sideways motion observed in 4/6 control embryos with a clearly labeled plasma membrane (Fig. 6C; see also Fig. 1A in Crowder et al., 2015).

In these simulations, 100% (n=99) of short flat spindles rotated to 90° (Movie 1) whereas only 3% (n=100) of long pointed spindles rotated to angles of 80-90°, balancing on the tip of the pointed pole (Fig. 6A). 97% of long pointed spindles partially rotated but became trapped with one flat side of the pole stably apposed to the cortex (Movie 2). Both axial ratios and starting angles are heterogeneous for real *mei-2(ct98)* spindles (Fig. 2A, C). However, 6/6 *mei-2(ct98)* spindles with axial ratios closest to 1.5 and with starting angles less than 45° became trapped in the partially rotated orientation, closely matching the simulation results. To separate axial ratio from pole shape, we ran simulations of imaginary short pointed spindles (Movie 3) and long flat spindles similar to *knl-1,3(kd)* spindles (Movie 4). 78% (n=100) of short pointed spindles rotated to 80-90°, balancing on the point of the spindle while 22% became trapped on one flat side of a pole (Fig. 6A). Thus an axial ratio of 0.9

significantly (p<.0001 Fisher's exact test) improved the success rate of rotation with pointed poles relative to an axial ratio of 1.5. Long flat spindles successfully rotated to 80-90° in 94% (n=100) of simulations and were trapped parallel to the cortex with isometric cortical pulling on both poles in only 6% of simulations. Thus flat poles significantly (p<.0001 Fisher's exact test) improved the efficiency of rotation to 90° relative to pointed spindles even with a constant axial ratio of 1.5, consistent with the improved rotation in *knl-1,3(kd)* compared with *mei-2(ct98)*.

We next considered why long pointed spindles never became trapped in a parallel orientation in our simulations as observed for 9/27 *mei-2(ct98)* embryos *in vivo*. From visual inspection of these partially rotated spindles (Fig. 6A bottom; Movie 2), it is obvious that astral microtubules are not long enough to reach from the cortex distal pole to the cortex and that to maximize pole-cortex contact on both poles, the spindle would have to bend. To address the role of astral microtubule length, we ran the same simulations but with the polymerization rate tripled from 0.06 μm/s to 0.18 μm/s (Fig. 6B; Movies 5-8). This polymerization rate is faster than that reported in cultured mammalian cells but still slower than that reported in *C. elegans* mitotic embryos (Srayko et al., 2005). The majority of simulated long pointed spindles with these longer astral microtubules still stalled in the partially rotated orientation (Movie 5). This matches the experimental results in that the real *mei-2(ct98)* spindles with axial ratios near 1.5 stalled in the partially rotated orientation and only spindles with much longer axial ratios stalled in the parallel orientation (Fig. 2A). In contrast, longer astral microtubules completely blocked rotation in 10% of short flat spindles and 55% of long flat spindles (Movie 6) by generating isometric cortical pulling on both poles. The rotation-promoting effect of a 0.9 axial ratio vs a 1.5 axial ratio for flat-poled spindles with longer astral microtubules was extremely

significant (p<.0001). Similar to the simulated long flat-poled spindles (Fig. 6B), 50% *knl-1,3(kd)* spindles with axial ratios near 1.5 became trapped in the parallel orientation (Fig. 2B). However, the other 50% of *knl-1,3(kd)* spindles partially rotated (Fig. 2B), in contrast with the other 45% of simulated long flat-poled spindles that successfully rotated to 80-90° (Fig. 6B). *knl-1,3(kd)* spindles, however, had narrower poles than the simulated flat-poles, which were modeled after wild-type poles (Fig. 2D). The simulations with longer astral microtubules thus solidified the conclusion that both short axial ratio and flat poles promote rotation.

To compare the time needed to reach a 60-90° perpendicular spindle orientation under different simulated conditions using ANOVA, we set the rotation time for those spindles that did not actually achieve a perpendicular orientation to 310 seconds (Fig. S1). Long spindles took significantly longer to rotate than short spindles with the same pole shape and pointed spindles took significantly longer to rotate than flat-poled spindles with the same axial ratio. This analysis again indicated that both short axial ratios and flattened poles can promote spindle rotation, but did not explain how the longest experimental *mei-2(ct98)* spindles became trapped in the parallel orientation.

mei-2(ct98) spindles have a low density of microtubules and bend to allow cortical capture of both spindle poles.

The finding that simulated long pointed spindles never became stalled in a parallel orientation prompted us to ask how the longest observed *mei-2(ct98)* spindles became stalled in the fully parallel orientation. Time-lapse imaging (Fig. 1A, B), as well as simulation results that include a "cortical glue", both indicated that the surface area of contact between pole LIN-5/dynein and cortical LIN-5/dynein is

maximized during rotation. Simulated long pointed spindles cannot maximize

contact between both poles and the cortex because of their fixed shape. 9/18 *mei-*

2(ct98) spindles bent back and forth during both metaphase and anaphase B (Fig.

7A). *mei-2(ct98)* spindles had a reduced density of both EBP-2::mKate, which tracks

growing plus ends of microtubules (Fig. 7B, C), and GFP::tubulin (Fig. 7D; see also

McNally et al., 2014). The combination of large axial ratio with reduced density of

microtubules likely allows spindle bending, which in turn allows both poles to come

into close enough proximity for stabilized cortical capture.

Viscous drag is responsible for rotation failure of simulated long flat-poled

spindles.

50% of long *knl-1,3(kd)* spindles (Fig. 2B) and 55% of simulated long flat-

poled spindles (Fig. 6B) failed to rotate. This is consistent with simulations of short

vs long flat-poled spindles with long astral microtubules which indicated that spindles

with a long axial ratio can remain parallel with both poles engaged in cortical pulling

for a longer period of time than spindles with a short axial ratio (Fig. S1). However,

the reason for this difference was not clear. The difference might be caused by

shape-dependent, steric masking of astral microtubules during rotation or it might be

caused by shape-dependent differences in viscous drag. In most simulations, astral

microtubules from both poles initially engaged the cortex, then one pole lost cortical

attachments before pivoting away from the cortex. If long spindles pivot more slowly

due to higher translational and rotational drag, this might allow more time for astral

microtubules from the departing pole to recapture the cortex. Our Cytosim models

used a cytoplasmic viscosity of 1 Pascal sec, determined from microrheology

(Daniels et al., 2006) and magnetic tweezers experiments (Garzon-Coral et al.,

2016) in *C. elegans* embryos. Both translational drag that depends on the radius of the spheres used to build the spindles and rotational drag that depends on the distance between spheres were incorporated into our Cytosim models. To determine whether viscosity might have an effect on spindle rotation, we ran simulations of short flat vs long flat spindles with long astral microtubules with a 10-fold reduction in viscosity (Movie 5). Rotation was completely rescued for long spindles (45% rotation at normal viscosity n=100; 100% rotation at reduced viscosity n=20) and this increased frequency of successful rotation by reducing viscosity was significant (p<.0001 Fisher's Exact test). In addition, the time until reaching 90° was not significantly different between short and long spindles at low viscosity (short: 188 ± 15 sec, n=11; long 164 ± 12 sec, n=20; p=.24 t test). In contrast, rotation of short flat spindles was relatively unaffected by reducing viscosity (10% failure n=100 vs 10% failure n=20; time to rotation high viscosity: 214 ± 6 sec n=99 vs low viscosity: 188 ± 15 sec n=20, p=.08 t test). This result demonstrated that shape dependent differences in viscous drag are the cause of rotation failure in simulations with long flat-poled spindles.

F-actin resists dynein-mediated cortical pulling.

F-actin can resist movement in a size and shape-dependent manner that is analogous but distinct from viscosity (Feric and Brangwynne, 2013). To experimentally test whether F-actin generates any measurable opposition to cortical pulling, we depleted profilin by RNAi to disassemble F-actin, and then analyzed its effects on late dynein-dependent spindle translocation in the kinesin-1 heavy chain mutant, *unc-116(f130)*. This Ala236Thr point mutation causes a temperature sensitive maternal effect lethal phenotype with the meiotic spindle completing

meiosis in the middle of the embryo. The metaphase spindle is further from the cortex than in *unc-116(RNAi)* or *kca-1(RNAi)* but can move to the cortex if dynein is hyper-activated by CDK-1 inhibition (Ellefson and McNally, 2011). Movement of the spindle to the cortex was also induced by depolymerizing F-actin by profilin (RNAi) (Fig. 8A, B). This result indicated that F-actin, which forms a deep cytoplasmic meshwork in meiotic embryos (Panzica et al., 2017), can oppose dynein-dependent cortical pulling.

Discussion

Our combined experimental and simulation results strongly support a model in which both short axial ratio (1 - 0.9) and slightly flattened spindle poles promote meiotic spindle rotation to a perpendicular orientation relative to the cortex. This perpendicular spindle orientation during anaphase is extremely conserved across animal phyla. The fact that the frequency of parallel anaphase matches the frequency of unhatched embryos for *mei-2(ct98)* supports the idea that perpendicular spindle orientation facilitates accurate extrusion of chromosomes into polar bodies. Short axial ratio with slightly flattened poles is conserved in other species with acentriolar female meiotic spindles such as humans (Holubcova et al., 2015) and even in species with centriole-bearing female meiotic spindles such as *Spisula solidissima* (McNally et al., 2016). *Drosophila* female meiotic spindles are naturally long and pointed during early metaphase, then shorten and round before rotating (Endow and Komma, 1997). Work on mouse oocytes has focused on the idea that meiotic spindles are positioned by an actin-driven and microtubule-independent mechanism (Mogessie et al., 2018), however, low doses of microtubule depolymerizing drugs inhibit meiosis II spindle rotation in mice (Ai et al., 2008a) and

rats (Ai et al., 2008b). Thus it is possible that cortical pulling on astral microtubules contributes to actin-driven mouse spindle rotation and it is also possible that spindle shape promotes cortical pulling by actomyosin on one spindle pole (Schuh and Ellenberg, 2008).

Our combined experimental and modeling results indicated that short spindles with slightly flattened poles promote accurate spindle rotation through three mechanisms. First, the round but slightly flattened shape of wild-type spindle poles during rotation maximizes the surface area of contact between pole dynein and cortical dynein. The increase in cortical dynein, dynactin and LIN-5 observed after pole contact would stabilize wild-type spindles in a perpendicular orientation and *mei-2(ct98)* spindles in a diagonal orientation. Second, short spindles are likely more rigid than long spindles and thus do not bend like *mei-2(ct98)* spindles. Spindle bending makes it possible for both poles of the longest *mei-2(ct98)* spindles to make close stable contact with the cortex. Third, the reduced viscous drag on a short spindle allows one pole to escape the cortex quickly so that astral microtubules from the escaping pole do not recapture the cortex. We previously calculated that the difference in rotational drag on spherical vs ellipsoid spindles would be very small relative to the force generated by a single dynein (Crowder et al., 2015) but reducing drag in our mathematical model dramatically rescued rotation of long spindles. The observed duration of astral microtubule contacts with the *C. elegans* cortex is very short due to catastrophes (Kozlowski et al., 2007) and in our model, rotation is mediated by successive, short duration pulling interactions. In this scenario, small differences in rotational velocity seem to have large effects on the probability of losing cortical pulling on one pole so that it can pivot away from the cortex. These three mechanisms are equally relevant for capture of spindle pole

dynein by microtubule plus ends emanating from the cortex as they are for capture of cortical dynein by astral microtubules.

An important issue is whether spherical spindle shape promotes spindle rotation or rotation promotes spherical shape. Spindle shortening occurs without cortical contact in embryos depleted of kinesin-1 (UNC-116) or its binding partner, KCA-1 (Yang et al., 2005) or simultaneously depleted of both kinesin-1 and dynein (Ellefson and McNally, 2009). Thus shortening is not caused by cortical pulling and shortening is not normally caused by cortical contact. In the very specific combination of *mei-2(ct98)* with mKate2::PH (which is localized at the cortex), spindle shortening and pole flattening occur after cortical contact and then allow rotation. These observations are all consistent with our model that spherical spindle shape promotes rotation by preventing cortical pulling on both spindle poles.

Our finding that long *mei-2(ct98); kca-1(RNAi)* spindles undergo sideways late translocation at the same velocity as short *kca-1(RNAi)* spindles might seem to contradict our finding that actin depolymerization facilitates late translocation of *unc-116(f130)* spindles. The first result suggests that shape-dependent drag is insignificant whereas the second results suggests that F-actin confers enough resistance to cortical pulling to block translocation across longer distances. The observed parallel spindle orientation during late translocation in *kca-1(RNAi)* embryos, as well as during early stages of rotation in control embryos, suggest that this movement is mediated by multiple dynein motors pulling on both poles. During this early stage of pulling on both poles, picoNewtons of drag would be much less than the picoNewtons of pulling. In our simulations, rotation initiates when one pole loses cortical pulling attachments. At this point the competition would not be between picoNewtons of dynein pulling and picoNewtons of drag. Instead, the

competition would be between the velocity of spindle pivoting and the probability of an astral microtubule recapturing the cortex through dynamic instability.

Parameters other than drag could also contribute to our results. If cortical microtubules are longer in *mei-2(ct98); kca-1(RNAi)* embryos, as reported for *mei-1(RNAi)* embryos (Kimura et al., 2017), then late translocation might be mediated by more microtubules extending between spindle poles and the cortex than in *kca-1(RNAi)* embryos. Likewise, recent work has shown that actin meshworks can inhibit microtubule polymerization in *Xenopus* extracts (Colin et al., 2018). Therefore the promotion of late translocation by actin depolymerization in *unc-116(f130)* embryos might be through an increase in the length of astral or cortical microtubules.

Understanding of the molecular mechanism of rotation would be improved by direct observation of the force-generating microtubule connections between the spindle and cortex. Pursuing a 3D model of rotation in which spindles are continuously shortening and clarification of the contribution of viscous drag from both experiment and modeling will also be essential.

Materials and Methods

C. elegans strains

Strains are listed in Table S1. The designation, *knl-1,3(kd)*, refers to either of two methods used. In the first method, strains with the endogenous *knl-1* and *knl-3* genes tagged with GFP were subjected to GFP(RNAi) by feeding for 48 hrs and mCherry::histone H2B with either LIN-5::mNeonGreen or DHC-1::mNeonGreen was imaged. Green fluorescence at kinetochores was undetectable in each time-lapse sequence. In the second method, strains with the endogenous *knl-1* and *knl-3* genes tagged with auxin-inducible degrons (Zhang et al., 2015) and bearing a TIR1

transgene were treated with auxin overnight. 13 *knl-1,3(kd)* time lapse sequences were of GFP(RNAi) worms and 17 were of auxin-treated degron worms. 23% of GFP(RNAi) spindles and 41% of auxin-treated degron spindles were elongated and underwent partial or no rotation, indicating that the extent of depletion is likely different between these methods. The number of GFP(RNAi) elongated non-rotating spindles (3) is too small for statistical comparison with the auxin-treated degron spindles (7). However, there is no overlap in the axial ratios of rotating and non-rotating spindles in Fig. 2B.

C. elegans genome editing

To tag KNL-1 at the C-terminus with GSGGSG-AID (flexible linker-auxin-inducible degron) and KNL-3 at the N-terminus with AID-GSG (auxin-inducible degron-flexible linker), PCR repair templates (consisting of 35-120 bp of homology flanking AID) were co-injected into JDW10 (*cpIs103[Psun-1>TIR1-C1::F2A::mTagBFP2-C1::NLS] II*) worms with purified Cas9-NLS, Cas9 universal tracrRNA, *dpy-10* crRNA, *dpy-10* ssODN repair template, and respective crRNAs as described (Paix et al., 2015).

knl-1 crRNA: RNA Sequence: 5'

UCGAAUGCUGGUGUUCUCUAGUUUUAGAGCUAUGCUGUUUUG 3'

knl-3 crRNA: RNA Sequence: 5'

CGCGGCUCUGACCGAGAAUGGUUUUAGAGCUAUGCUGUUUUG 3'

In utero live imaging

L4 larvae were incubated overnight at 25°C, then adult hermaphrodites were anesthetized with tricaine/tetramisole as described (Kirby et al., 1990; McCarter et al., 1999) and gently mounted between a coverslip and a thin 3% agarose pad on a slide. Time lapse images were acquired at 15 sec intervals with a Solamere

spinning disk confocal equipped with a Yokogawa CSU10, Hamamatsu ORCA FLASH 4.0 CMOS detector, Olympus 100X/1.35 objective and MicroManager software control.

Fixed immunofluorescence

C. elegans meiotic embryos were extruded from hermaphrodites in 0.8× egg buffer by gently squishing of worms between coverslip and slide, flash frozen in liquid N2, permeabilized by removing the coverslip, and then fixed in cold methanol before staining with antibodies and DAPI. Primary antibodies used in this work were mouse monoclonal anti-tubulin (DM1α; Sigma-Aldrich; 1:200 dilution). Secondary antibodies used were Alexa Fluor 488 anti–mouse (Molecular Probes; 1:200 dilution). Complete z stacks were captured for each meiotic embryo with an inverted microscope (Olympus IX81) equipped with a 60× PlanApo 1.42 objective, a disk-scanning unit (Olympus), and a Hamamatsu ORCA Flash 4.0 CMOS detector and controlled with MicroManager software.

RNAi

RNAi depletion of GFP, KCA-1 and PFN-1 was carried out by feeding HT115 bacteria transformed with L4440-based plasmids (Kamath et al., 2003).

Spindle rotation simulations

The complete models are included in Online Supplemental Material. Our agent-based simulations of spindle rotation were run on Cytosim, a stochastic physics simulator specializing in cytoskeletal cellular processes. Simulations are set within a 2-dimensional representation of a *C. elegans* zygote built as a capsule (rectangle with hemispheres capping off two opposing sides) with hemisphere radii of 15 microns and rectangular length of 10 microns. Viscosity within the cell is set to 1 Pa.s, approximately the viscosity of an embryo, and temperature is set to 25°C.

Within this environment steric interactions are enabled, ensuring that solid objects including the spindle and microtubules cannot occupy the same space. Two different microtubule types are simulated. First, cortical microtubules nucleating and remaining stable in length at 200 nanometers. Astral microtubules are nucleated from spindle poles and exhibit dynamic instability, reaching lengths of up to a few microns before catastrophe and rescue. At the onset of simulation the spindles are built as solid objects, made up of several solid bead-like structures to approximate the shape of a spindle that is either a) shortened with flat poles, b) shortened with pointed poles, c) long with flat poles, or d) long with pointed poles. Spindles are assembled so that their pole-to-pole axis is tangential to the hemisphere center, these are placed in this orientation approximately 1.5-2 microns away from the edge of the cell, perfectly centered to the hemisphere. Spindle poles are defined in the simulation by a series of points that act as microtubule nucleators, the spatial positions of these points are user-defined in relation to the origin of the spindle solid object, ensuring that as the spindle moves in simulation space the spindle poles move with it. The cell-space edge proximal to the spindle is seeded with 140 cortical microtubule nucleators which are fixed in space in the shape of the cell boundary. This same space is seeded with "cortical glue" agents that bind the astral microtubules tightly to mimic the observation that once spindles rotate one pole to the cortex they remain in that position. (20 simulations without this cortical glue were run for short and long spindles with flat poles. Results were not significantly different with or without cortical glue. Short spindles p = 1.0; long spindles p= 0.06 Fisher's exact test.) Finally, 2000 dynein motors, which can bind cortical microtubules (mimicking dynein at the cortex) but also bind and motor along astral microtubules (mimicking spindle pole dynein), are added to the entire simulation space and

allowed to diffuse around freely. Dyneins, represented as red dots, bind microtubules (white lines) and pull the spindle along. If the spindle reaches the cortex with its astral microtubules they are bound by the "cortical glue" (purple dots). Each simulation is allowed to run for 300 simulated seconds (300,000 frames at 1 millisecond per frame).

ACKNOWLEDGEMENTS

We thank Reto Gassmann, Sander van den Heuvel, Arshad Desai and Paul Mains for strains. Some strains were provided by the Caenorhabditis Genetics Center, which is funded by NIH Office of Research Infrastructure Programs (P40 OD010440). We thank Francois Nedelec for help utilizing Cytosim and Lesilee Rose for critical reading of the manuscript.

COMPETING INTERESTS

The authors declare no competing interests.

AUTHOR CONTRIBUTIONS

E.V., K. M., B. D., Q. L. and M.T.P: design and execution of experiments and analysis of results. D.B.C.: Mathematical modeling. A.S.M and F.J.M: Experimental design, data analysis and writing.

FUNDING

REFERENCES

Ai, J., Wang, Q., Li, M., Shi, L., Ola, S., Xiong, B., Yin, S., Chen, D. and Sun, Q. (2008). Roles of microtubules and microfilaments in spindle movements during rat oocyte meiosis. *J Reprod Dev.* **54,** 391-396.

Ai, J., Wang, Q., Yin, S., Shi, L., Xiong, B., OuYang, Y., Hou, Y., Chen, D., Schatten, H. and Sun, Q. (2008). Regulation of peripheral spindle movement and spindle rotation during mouse oocyte meiosis: new perspectives. *Microsc. Microanal.* **14**, 349-356.

Albertson, D. G. and Thomson, J. N. (1993). Segregation of holocentric chromosomes at meiosis in the nematode, *Caenorhabditis elegans. Chromosome Res.* **1,** 15-26.

Colin, A., Singaravelu, P., Théry, M., Blanchoin, L. and Gueroui, Z. (2018). Actin-network architecture regulates microtubule dynamics. *Curr Biol.* **28,** 2647-2656.

Connolly, A. A., Osterberg, V., Christensen, S., Price, M., Lu, C., Chicas-Cruz, K., Lockery, S., Mains, P. E., and Bowerman B. (2014). *Caenorhabditis elegans* oocyte meiotic spindle pole assembly requires microtubule severing and the calponin homology domain protein ASPM-1. *Mol Biol Cell.* **25,** 1298-1311.

Crowder, M. E., Flynn, J. R., McNally, K. P., Cortes, D. B., Price, K. L., Kuehnert, P.A., Panzica, M. T., Andaya, A., Leary, J. A. and McNally, F. J. (2015). Dynactin-dependent cortical dynein and spherical spindle shape correlate temporally with meiotic spindle rotation in *Caenorhabditis elegans*. *Mol Biol Cell.* **26,** 3030-3046.

Daniels, B. R., Masi, B. C. and Wirtz, D. (2006). Probing single-cell micromechanics in vivo: the microrheology of *C. elegans* developing embryos. *Biophys J.* **90,** 4712-9.

Dorn, J.F., Zhang, L., Paradis, V., Edoh-Bedi, D., Jusu, S., Maddox, P.S. and Maddox, A.S. (2010). Actomyosin tube formation in polar body cytokinesis requires anillin in *C. elegans*. *Curr. Biol.* **20,** 2046-2051.

Dumont, J., Oegema, K. and Desai, A. (2010). A kinetochore-independent mechanism drives anaphase chromosome separation during acentrosomal meiosis. *Nat Cell Biol.* **12,** 894-901.

Ellefson, M. L. and McNally, F.J. (2009). Kinesin-1 and cytoplasmic dynein act sequentially to move the meiotic spindle to the oocyte cortex in *Caenorhabditis elegans*. *Mol Biol Cell.* **20,** 2722-2730.

Ellefson, M. L. and McNally, F. J. (2011). CDK-1 inhibits meiotic spindle shortening and dynein-dependent spindle rotation in *C. elegans*. *J Cell Biol.* **193,** 1229-1244.

Endow, S. A. and Komma, D. J. (1997). Spindle dynamics during meiosis in *Drosophila* oocytes. *J Cell Biol.* **137,** 1321-36.

Fabritius, A. S., Ellefson, M. L. and McNally, F. J. (2011a). Nuclear and spindle positioning during oocyte meiosis. *Curr Opin Cell Biol.* **23,** 78-84.

Fabritius, A. S., Flynn, J. R. and McNally, F. J. (2011b). Initial diameter of the polar body contractile ring is minimized by the centralspindlin complex. *Dev Biol.* **359,** 137-148.

Feric, M. and Brangwynne, C. P. (2013). A nuclear F-actin scaffold stabilizes ribonucleoprotein droplets against gravity in large cells. *Nat Cell Biol.* **15,** 1253-9.

Garzon-Coral, C., Fantana, H.A., and Howard, J. (2016) A force-generating machinery maintains the spindle at the cell center during mitosis. Science. **352**, 1124-1127.

Holubcová, Z., Blayney, M., Elder, K. and Schuh, M. (2018). Human oocytes. Error-prone chromosome-mediated spindle assembly favors chromosome segregation defects in human oocytes. *Science.* **348,** 1143-7.

Kamath, R. S., Fraser, A. G., Dong, Y., Poulin, G., Durbin, R., Gotta, M., Kanapin, A., Le Bot, N., Moreno, S., Sohrmann, M. , et al. (2003). Systematic functional analysis of the *Caenorhabditis elegans* genome using RNAi. *Nature.* **421,** 231-237.

Kimura, K., Mamane, A., Sasaki, T., Sato, K., Takagi, J., Niwayama, R., Hufnagel, L., Shimamoto, Y., Joanny, J. F., Uchida, S. and Kimura, A. (2017). Endoplasmic-reticulum-mediated microtubule alignment governs cytoplasmic streaming. *Nat Cell Biol.* **19,** 399-406.

Kirby, C., Kusch, M. and Kemphues, K. (1990). Mutations in the par genes of *Caenorhabditis elegans* affect cytoplasmic reorganization during the first cell cycle. *Dev. Biol.* **142,** 203-215.

Kline-Smith, S. L. and Walczak, C. E. (2002). The microtubule-destabilizing kinesin XKCM1 regulates microtubule dynamic instability in cells. *Mol Biol Cell.* **13,** 2718-31.

Kotak, S. (2019). Mechanisms of spindle positioning: lessons from worms and mammalian cells. *Biomolecules.* **9,** pii, E80.

Kozlowski, C., Srayko, M. and Nedelec, F. (2007). Cortical microtubule contacts position the spindle in *C. elegans* embryos. *Cell.* **129,** 499-510.

McCarter, J., Bartlett, B., Dang, T. and Schedl, T. (1999). On the control of oocyte meiotic maturation and ovulation in *Caenorhabditis elegans. Dev. Biol.* **205,** 111-128.

McNally, F. J. (2013). Mechanisms of spindle positioning. *J Cell Biol.* **200,** 131-140.

McNally, K., Audhya, A., Oegema, K. and McNally, F. J. (2006). Katanin controls mitotic and meiotic spindle length. *J Cell Biol.* **175,** 881-891.

McNally, K., Berg, E., Cortes, D. B., Hernandez, V., Mains, P. E. and McNally, F. J. (2014). Katanin maintains meiotic metaphase chromosome alignment and spindle structure in vivo and has multiple effects on microtubules in vitro. *Mol Biol Cell.* **25,** 1037-49.

McNally, K. L., Martin, J. L., Ellefson, M. and McNally, F. J. (2010). Kinesin-dependent transport results in polarized migration of the nucleus in oocytes and inward movement of yolk granules in meiotic embryos. *Dev Biol.* **339,** 126-140.

McNally, K. P., Panzica, M. T., Kim, T., Cortes, D. B. and McNally, F. J. (2016). A novel chromosome segregation mechanism during female meiosis. *Mol Biol Cell.* **27,** 2576-89.

Mogessie, B., Scheffler, K. and Schuh, M. (2018). Assembly and positioning of the oocyte meiotic spindle. *Annu Rev Cell Dev Biol.* **34,** 381-403.

Nedelec, F. and Foethke, D. (2007). Collective Langevin dynamics of flexible cytoskeletal fibers. *N. J. Phys.* **9,** 427.

Paix, A., Folkmann, A., Rasoloson, D. and Seydoux, G. (2015). High Efficiency, Homology-Directed Genome Editing in Caenorhabditis elegans Using CRISPR-Cas9 Ribonucleoprotein Complexes. *Genetics.* **201**, 47-54.

Panzica, M. T., Marin, H. C., Reymann, A. C. and McNally, F. J. (2017). F-actin prevents interaction between sperm DNA and the oocyte meiotic spindle in *C. elegans. J Cell Biol.* **216,** 2273-2282.

Sathananthan, A. H. (1985). Maturation of the human oocyte in vitro: nuclear events during meiosis (An ultrastructural study). *Gamete Res.* **12**, 237-254.

Schuh, M. and Ellenberg, J. (2008). A new model for asymmetric spindle positioning in mouse oocytes. *Curr Biol.* **18,** 1986-1992.

Srayko, M., Kaya, A., Stamford, J. and Hyman, A. A. (2005). Identification and characterization of factors required for microtubule growth and nucleation in the early *C. elegans* embryo. *Dev Cell.* **9,** 223-236.

Szollosi, D., Calarco, P., and Donahue, R.P. (1972). Absence of centrioles in the first and second meiotic spindles of mouse oocytes. *J Cell Sci.* **11**, 521-541;

Tan, R., Foster, P. J., Needleman, D. J. and McKenney, R. J. (2018). Cooperative accumulation of dynein-dynactin at microtubule minus-ends drives microtubule network reorganization. *Dev Cell.* **44,** 233-247.

van der Voet, M., Berends, C. W., Perreault, A., Nguyen-Ngoc, T., Gonczy, P., Vidal, M., Boxem, M. and van den Heuvel, S. (2009). NuMA-related LIN-5, ASPM-

1, calmodulin and dynein promote meiotic spindle rotation independently of cortical LIN-5/GPR/Galpha. *Nat Cell Biol.* **11,** 269-277.

Yang H. Y., McNally, K. and McNally, F. J. (2003). MEI-1/katanin is required for translocation of the meiosis I spindle to the oocyte cortex in *C. elegans*. *Dev Biol.* **260,** 245-259.

Yang, H. Y., Mains, P. E. and McNally, F.J. (2005). Kinesin-1 mediates translocation of the meiotic spindle to the oocyte cortex through KCA-1, a novel cargo adapter. *J Cell Biol.* **169**, 447-457.

Zhang, L., Ward, J. D., Cheng, Z., and Dernburg, A. F. (2015). The auxin-inducible degradation (AID) system enables versatile conditional protein depletion in *C. elegans*. *Development.* **142**, 4374-4384.

FIGURES
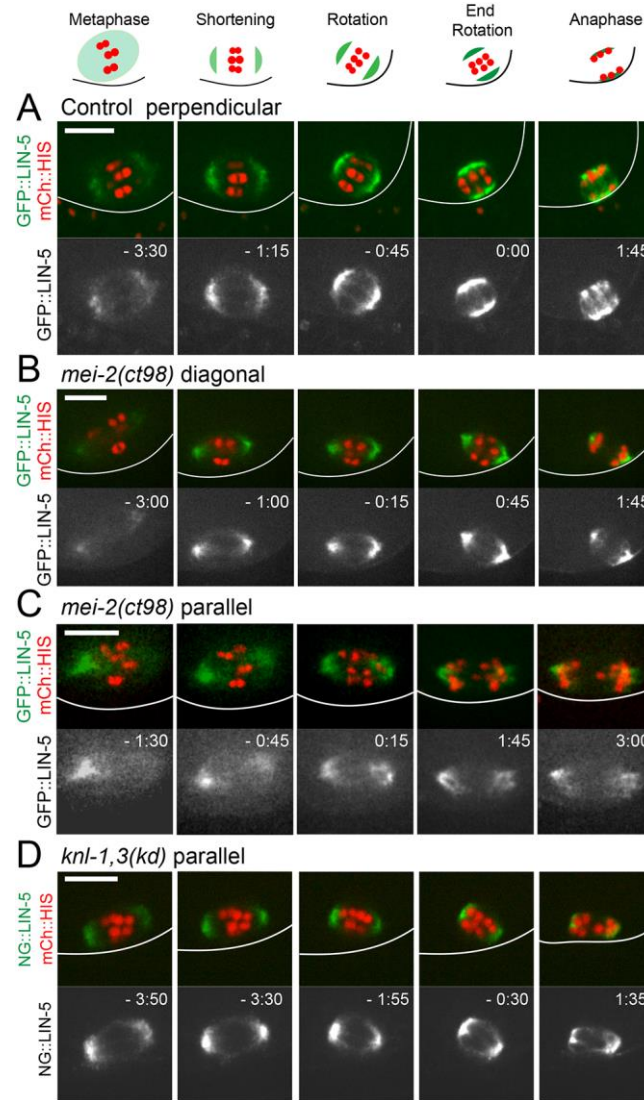
Figure 1. *mei-2(ct98)* and *knl-1,3(kd)* meiotic spindles are defective in APC-

dependent rotation. (A) Time-lapse images of a control embryo expressing

GFP::LIN-5 and mCherry::Histone (mCh::HIS) show the progression of the spindle

from metaphase to the end of anaphase A. (B) A spindle in a *mei-2(ct98)* embryo

expressing GFP::LIN-5 and mCherry::Histone undergoes a partial rotation. (C) A

spindle in a *mei-2(ct98)* embryo expressing GFP::LIN-5 and mCherry::Histone fails

to rotate and remains parallel to the cortex during anaphase. (D) A spindle in a *knl-1,3(kd)* embryo expressing mNeonGree:LIN-5 and mCherry::Histone fails to rotate and remains parallel to the cortex during anaphase. Images were captured every 15 seconds. Time 0 is 15 seconds prior to the observed start of chromosome separation. This corresponds

approximately to the start of rotation in control embryos. Bars, 6 µm.
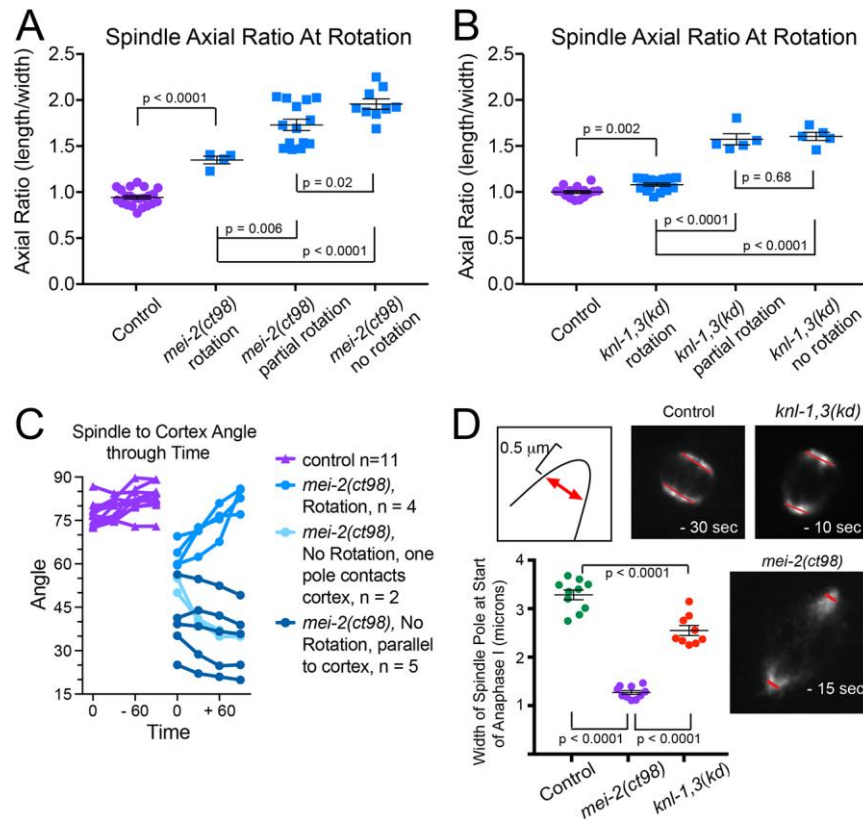
Figure 2. Spindle rotation is affected by both the axial ratio and pole width. (A) Axial ratios of control and *mei-2(ct98)* spindles that rotated, partially rotated or failed to rotate were measured 15 seconds prior to the start of chromosome segregation. Average axial ratios were: Control, 0.93 ± 0.02 n=22; *mei-2(ct98)* that rotated, 1.34 ± 0.04 n=4; *mei-2(ct98)* that partially rotated, 1.72 ± 0.06 n=14; *mei-2(ct98)* that did not rotate, 1.95 ± 0.06 n=9. (B) Axial ratios of control and *knl-1,3-(kd)* spindles were measured 10 seconds prior to the start of chromosome segregation. Average axial ratios were: Control, 0.98 ± 0.02 n=15; *knl-1,3-(kd)* that rotated, 1.06 ± 0.02 n=15; *knl-1,3-(kd)* that partially rotated, 1.56 ± 0.06 n=5; *knl-1,3-(kd)* that did not rotate, 1.56 ± 0.04 n=5. Partial rotation was defined as 15-80° in A and B. (C) Spindle to cortex angle was measured in time-lapse images, captured at 15 second intervals, of embryos expressing GFP::DNC-2. t=0 is when a pole touched the cortex. (D)

Spindle pole width (red arrow) was measured 0.5 µm from the outermost edge of the spindle at the start of chromosome separation. Average widths were: control, 3.28 ± 0.10 n=10; *mei-2(ct98)*, 1.25 ± 0.04 n=10; *knl-1,3-(kd)*, 2.54 ± 0.10 n=9. p values in A and B are from Student's t test. Error bars indicate standard error of the mean.
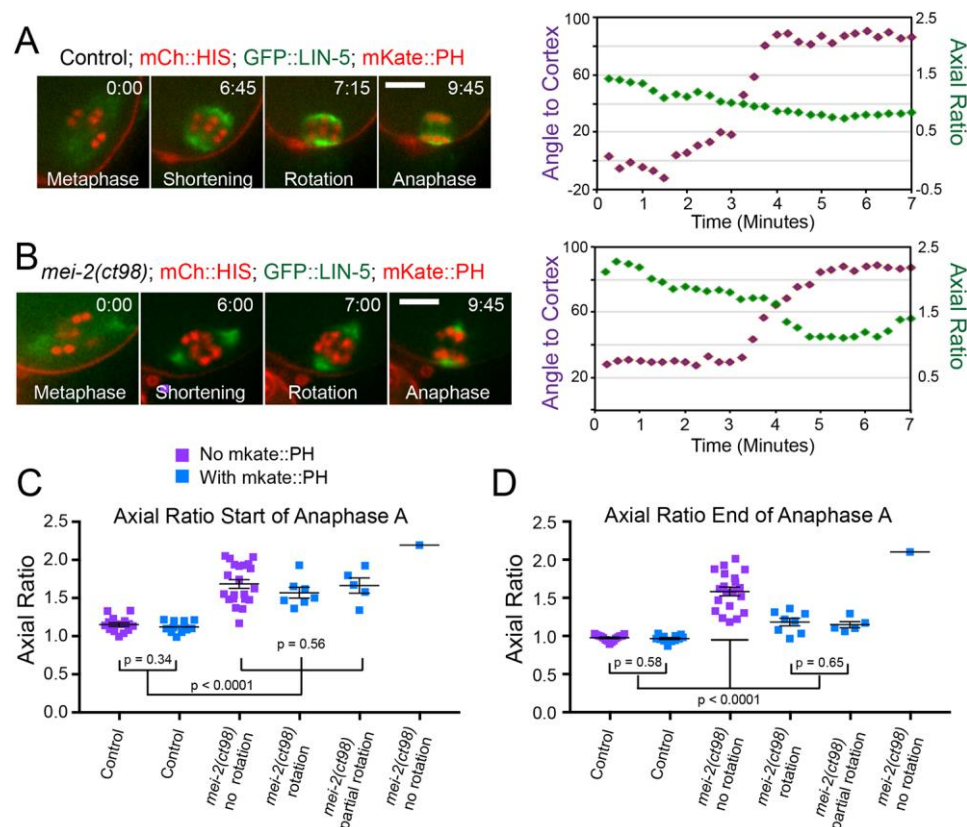
Figure 3. The rotation defect in *mei-2(ct98)* embryos is suppressed by an mKate::PH transgene. (A) Representative time-lapse images are shown for a control embryo expressing mCherry::Histone, GFP::LIN-5 and mKate::PH. A plot of both axial ratio and spindle to cortex angle over time indicates that rotation began when the axial ratio was 1.0 and was completed within 60 seconds. (B) Time-lapse images captured from a *mei-2(ct98)* embryo expressing mKate::PH as well as mCherry::Histone and GFP::LIN-5 show that spindle rotation began when the axial ratio was 1.72 and but did not complete until after the axial ratio reached 1.0. (C) Axial ratios are shown for control and *mei-2(ct98)* spindles at the start of chromosome separation. Control, no PH: 1.13 ± 0.03, n=15; control with PH: 1.09 ± 0.02, n=12; *mei-2(ct98)*, no PH: 1.66 ± 0.06, n=21; *mei-2(ct98)* with PH, rotated: 1.54 ± 0.07, n=7; *mei-2(ct98)* with PH, partially rotated: 1.64 ± 0.10, n=5. (D) Axial ratios

of control and *mei-2(ct98)* spindles at the end of anaphase A. Control, no PH: 0.95 ±

0.01, n=15; control with PH: 0.93 ± 0.01, n=12; *mei-2(ct98)*, no PH: 1.55 ± 0.06,

n=20; *mei-2(ct98)* with PH, rotated: 1.15 ± 0.05, n=8; *mei-2(ct98)* with PH, partially

rotated: 1.12 ± 0.04, n=5. Partial rotation was defined as 60-80° in C and D to

clearly show the extent of suppression by mKate::PH. p value is from Student's t
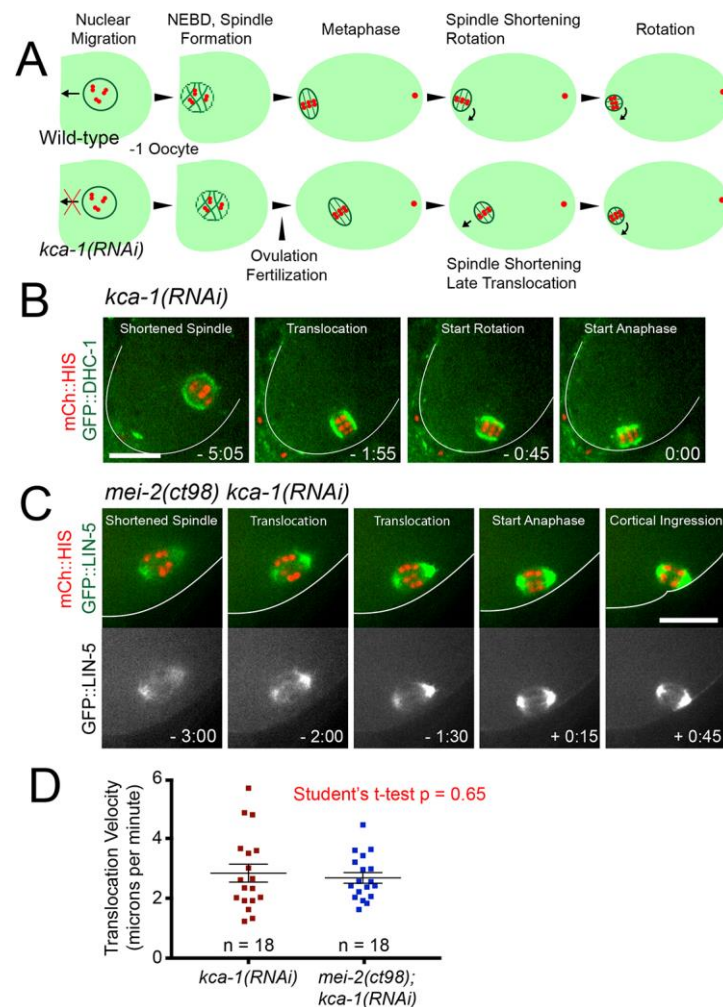
test. Error bars indicate standard error of the mean.

Figure 4. Dynein-dependent pulling forces are wild-type in *mei-2(ct98)* embryos. (A) Cartoon depiction of nuclear and spindle movements in wild-type and KCA-1-depleted worms. In wild-type oocytes, the nucleus migrates to the cortex immediately prior to nuclear envelope breakdown. The MI spindle forms and remains somewhat parallel to the cortex until APC activation and rotation. In a KCA-1-depleted embryo, nuclear migration fails and the spindle undergoes a late, dynein-dependent translocation to the

cortex prior to rotation. (B) Time-lapse images of a *kca-1(RNAi)* embryo correspond to the spindle stages shown in (A). (C) In a *mei-2(ct98); kca-1(RNAi)* embryo the

spindle undergoes a late translocation followed by a partial rotation. (D) Late translocation velocities are similar in *kca-1(RNAi)* embryos (2.83 ± 0.30 s.e.m., n=18), and *mei-2(ct98); kca-1(RNAi)* embryos (2.67 ± 0.18 s.e.m, n=18). Times in (B) and (C) are relative to the start of chromosome separation. Bars, 10 μm. Error bars indicate standard error of the mean.
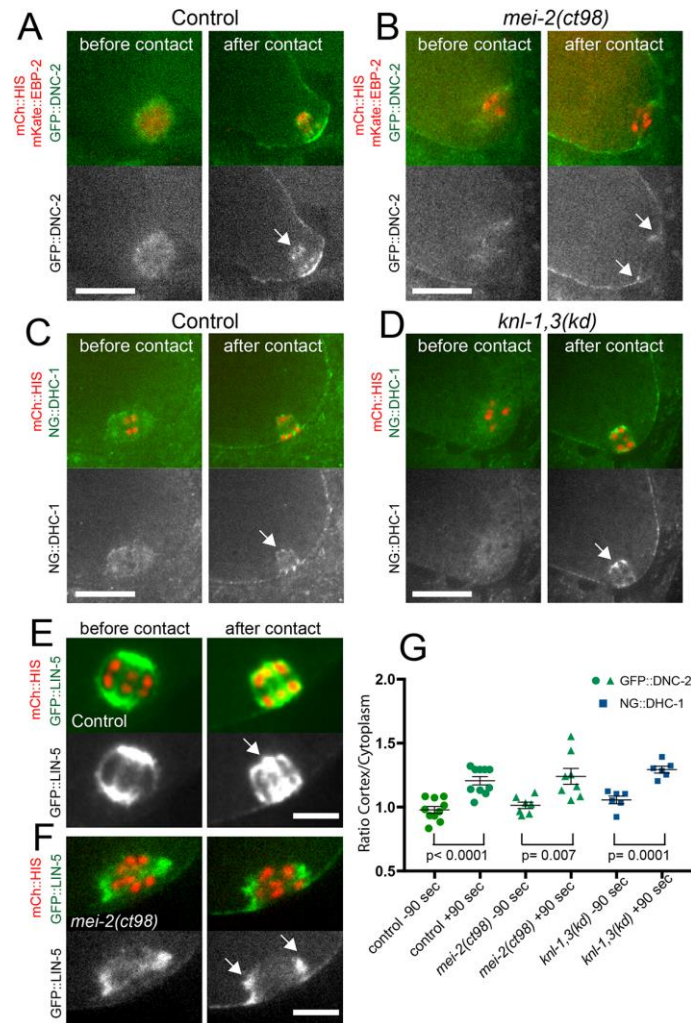
Figure 5. Endogenously tagged dynein regulators label spindle poles and cortices in control, *mei-2(ct98)* and *knl-1,3(kd)* embryos. (A, B). Cortical GFP::DNC-2 (p50 dynamitin) increases in intensity as spindles shorten and rotate in control (A) and *mei-2(ct98)* (B) embryos. (C, D) Cortical mNeonGreen::dynein heavy chain (NG::DHC-1) increases in intensity as spindles shorten and rotate in control (C) and *knl-1,3(kd)* (D) embryos. (E, F) Cortical GFP::LIN-5 increases after spindle pole

contact with the cortex in control (E) and *mei-2(ct98)* (F) embryos. (G) Ratio of cortical/cytoplasmic fluorescence intensity. P values from Student's t test. Bars (A-D) 10 μm, (E, F) 4 μm. Error bars indicate standard error of the mean. White arrows indicate spindle poles.
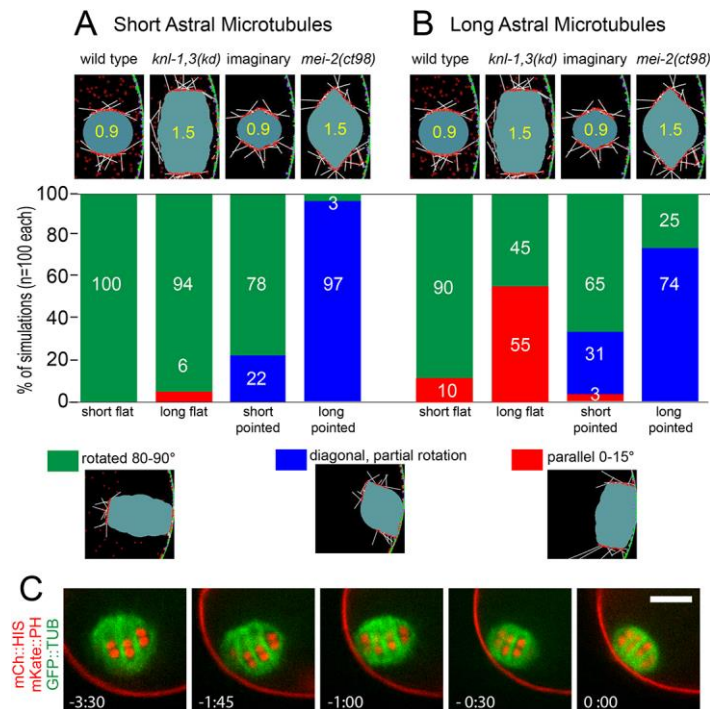
Figure 6. Simulations reveal that both short axial ratios and flattened spindle poles contribute to successful rotation to 90°. A) and B) Frequency of successful rotation to 90° during 300 second Cytosim simulations with spindles of different shapes. n=100 simulations for each of 8 conditions. C) Time-lapse sequence of a real rotation event showing that the spindle initially moves sideways toward the cortex before rotating. Bar = 5 μm.
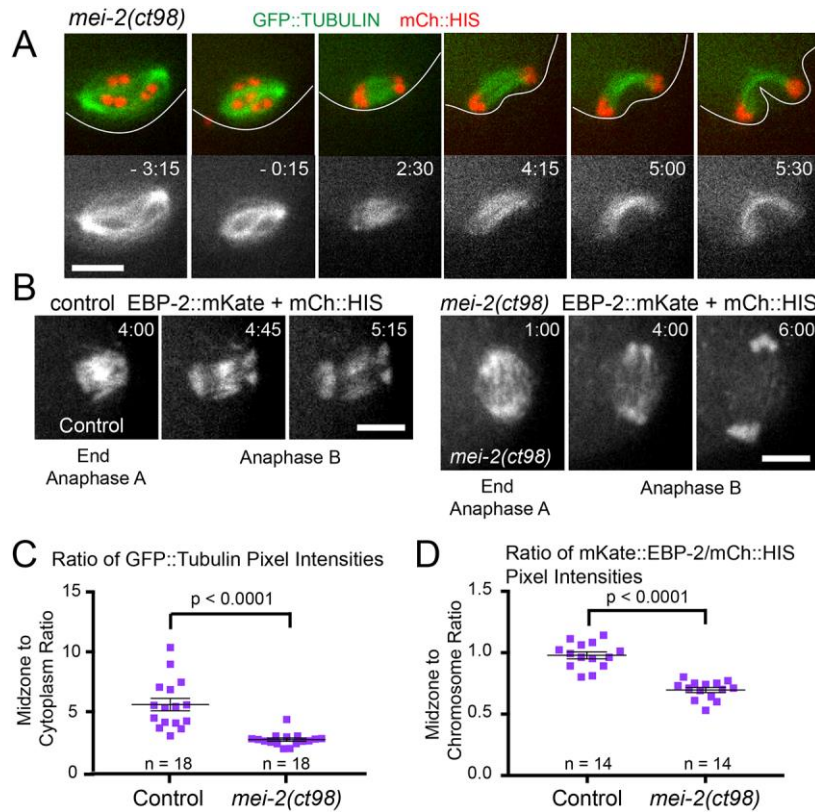
Figure 7. Both spindle poles in *mei-2(ct98)* spindles can interact with the cortex because low MT and EBP-2 density in the midzone allows them to bend. (A) Time-lapse images of a *mei-2(ct98)* embryo expressing GFP::tubulin and mCherry::Histone shows a spindle which is parallel to the cortex and which bends before and during anaphase. Time is relative to the start of chromosome separation. Bar, 6μm. (B) Time-lapse images of control and *mei-2(ct98)* embryos expressing EBP-2::mKate2 and mCherry::Histone. Bars, 4μm. (C) Mean GFP::tubulin pixel intensity for the midzone and the cytoplasm was measured when the chromosomes were 4-5μm apart and background subtracted. The average ratio for the control was 5.84 ± 0.63 s.e.m.; the average *mei-2(ct98)* ratio was 2.84 ± 0.21 s.e.m. (D) Mean

EBP-2::mKate2 pixel intensity in the midzone and mean mCherry::Histone pixel intensity were measured when the chromosomes were 4-5μm apart. The average ratio for the control was 0.98 ± 0.03 s.e.m.; the average ratio for *mei-2(ct98)* was 0.69 ± 0.02 s.e.m. Error bars indicate standard error of the mean.
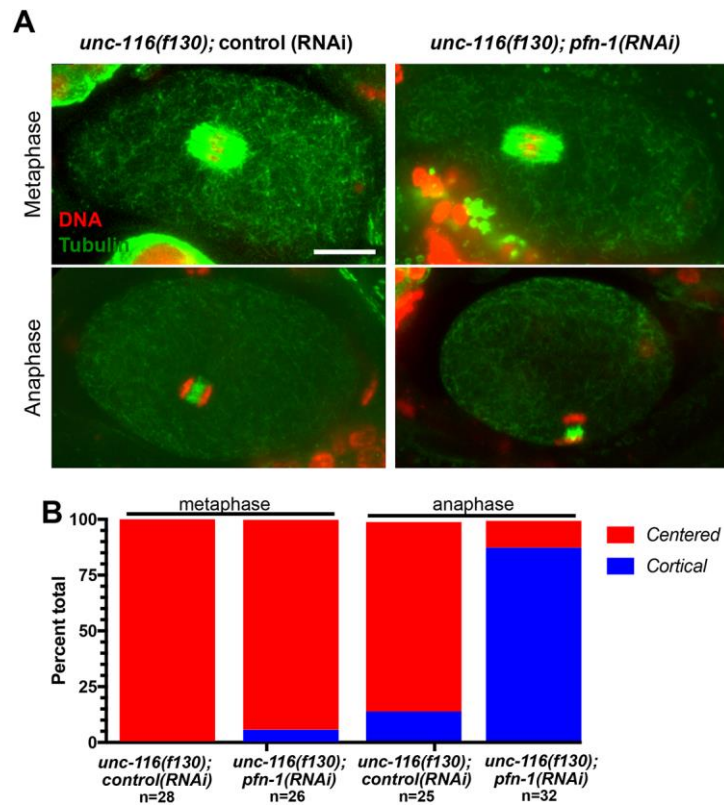
Figure 8. Depletion of F-actin rescues dynein-dependent late spindle translocation in *unc-116(f130)* meiotic embryos. (A) Representative images of embryos grown at 25°C, fixed and stained with anti-tubulin antibodies. Bar, 10 μm. (B) Quantification of the frequency of centered or cortical spindle position at metaphase and anaphase.
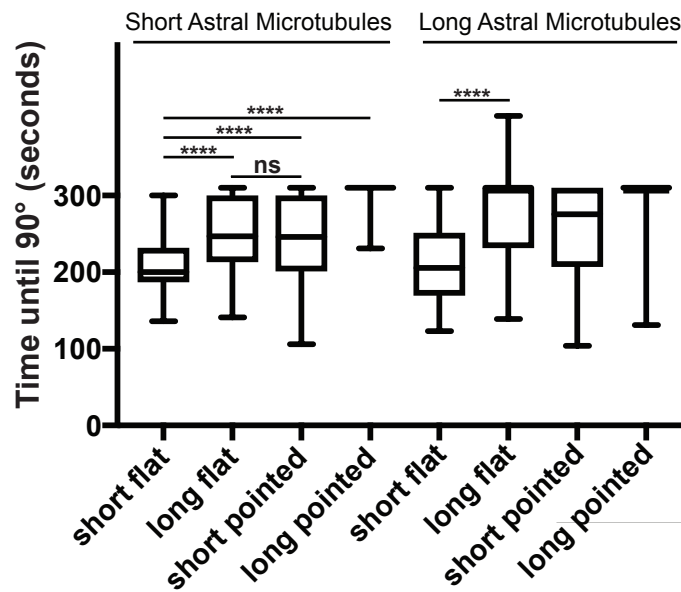
Figure S1. Both short axial ratio and flat spindle poles decrease the time required to rotate to 90° in Cytosim simulations. Spindles that did not rotate to 90° during the 300 sec simulation were assigned a time of 310 sec. n=100 simulations for each of 8 conditions. Boxes extend from the 25th to the 75th percentile.
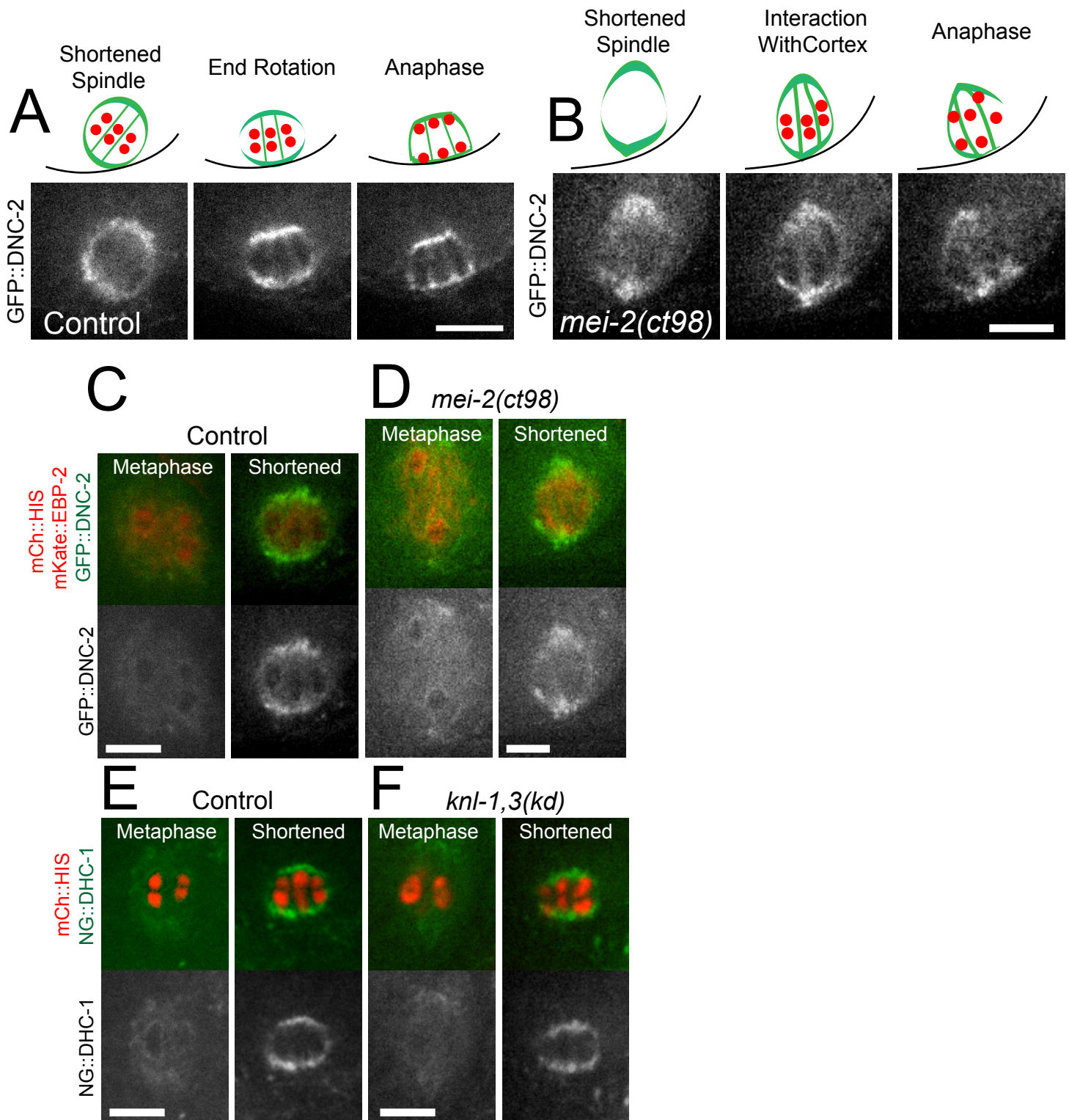**** indicates p<.0001 by ANOVA.

Figure S2. Endogenously tagged dynein regulators label spindle poles in control, *mei-2(ct98)* and *knl-1,3(kd)* embryos. (A-D). GFP::DNC-2 (p50 dynamitin) is present at spindle poles in control (A, C) and *mei-2(ct98)* (B, D) embryos. (E-F). mNeonGree::DHC-1 is present at spindle poles of control (E) and *knl-1,3(kd)* spindles (F).
Bars = 5 μm.

Table S1. *C. elegans* strains.

FM125: *ruIs57[pie-1p::GFP::tubulin + unc-119(+)]V; itIs37[pie-1p::mCherry:H2B::pie-1 3'UTR + unc-119(+)] IV.*

FM13: *mei-2(ct98) I; ruIs57[pie-1p::GFP::tubulin + unc-119(+)]V; itIs37[pie-1p::mCherry:H2B::pie-1 3'UTR + unc-119(+)] IV.*

FM562: *lin-5(he244[egfp::lin-5] II; itIs37[pie-1p::mCherry:H2B::pie-1 3'UTR + unc-119(+)] IV.*

FM582: *mei-2(ct98) I; lin-5(he244[egfp::lin-5] II; itIs37[pie-1p::mCherry:H2B::pie-1 3'UTR + unc-119(+)] IV.*

FM485: *lin-5(he244[egfp::lin-5] II; duSi10[mex-5p::mCherry::H2B operon linker mKate2::PH inserted in K03H6.5] IV.*

FM583: *mei-2(ct98) I; lin-5(he244[egfp::lin-5] II; duSi10[mex-5p::mCherry::H2B operon linker mKate2::PH inserted in K03H6.5] IV.*

FM461: *cpIs54[mex-5p::mKate::PLC(delta)PH(A735T)::tbb-2 3'UTR + unc-119(+)] II; itIs37[pie-1p::mCherry:H2B::pie-1 3'UTR + unc-119(+)] IV; ruIs57[pie-1p::GFP::tubulin + unc-119(+)] V.*

EU1561: *orIs17 [dhc-1::GFP::DHC-1, unc-119(+)]; itIs37 [unc-119(+) pie-1::mCherry::H2B] IV.*

FM460: *prtSi122[pRG629; mex-5p::ebp-2::mKate2::tbb-2 3'UTR + unc-119(+)] II; dnc-2[prt42(N-terminal 3XFLAG::GFP)] III; itIs37[pie-1p::mCherry:H2B::pie-1 3'UTR + unc-119(+)] IV.*

FM462: *mei-2(ct98) I; prtSi122[pRG629; mex-5p::ebp-2::mKate2::tbb-2 3'UTR + unc-119(+)] II; dnc-2[prt42(N-terminal 3XFLAG::GFP)] III; itIs37[pie-1p::mCherry:H2B::pie-1 3'UTR + unc-119(+)] IV.*

HR399: *unc116(f130) unc-36(e251) III*

FM568: *lin-5(cp288[lin-5::mNG-C1^3xFlag]) II; knl-1(lt53[knl-1::GFP::tev::loxP::3xFlag]))III; itIs37 [pie-1p::mCherry::H2B::pie-1 3'UTR + unc-119(+)] IV; knl-3 (lt46 [GFP::knl-3]) V*

FM593: *dhc-1(cp268[dhc::mNG-C1^3xFlag]) I; knl-1(lt53[knl-1::GFP::tev::loxP::3xFlag]))III; itIs37 [pie-1p::mCherry::H2B::pie-1 3'UTR + unc-119(+)] IV; knl-3 (lt46 [GFP::knl-3]) V*

FM553: *cpIs103[Psun-1>TIR1-C1::F2A::mTagBFP2-C1::NLS + SEC] II; knl-1(du5 [KNL-1::AID]) III; itIs37 [pie-1p::mCherry::H2B::pie-1 3'UTR + unc-119(+)] IV; ruIs57 [pie-1p::GFP::tubulin + unc-119(+)] V; knl-3(du2 [AID::KNL-3]) V*

FM554: *ASPM-1(or1935 [GFP::ASPM]) I; cpIs103[Psun-1>TIR1-C1::F2A::mTagBFP2-C1::NLS + SEC] II; knl-1(du5 [KNL-1::AID]) III; itIs37 [pie-1p::mCherry::H2B::pie-1 3'UTR + unc-119(+)] IV; knl-3(du2 [AID::KNL-3]) V*

FM594: *dhc-1(cp268[dhc::mNG-C1^3xFlag]) I; itIs37 [pie-1p::mCherry::H2B::pie-1 3'UTR + unc-119(+)] IV*

FM595: *lin-5(cp288[lin-5::mNG-C1^3xFlag]) II; itIs37 [pie-1p::mCherry::H2B::pie-1 3'UTR + unc-119(+)] IV*

Cytosim code

%%%%%%%%%%%%%%%%%%%%%%%%%%%%%% SIM %%%%%%%%%%%%%%%%%%%%%%%%%%%%%%%%%

```
set simul INVIVO          %Parameters that describe the simulation physics
{
    time_step = 0.001     %The time interval, in seconds, that passes between each timepoint calculated by the Langevin
    steric = 1, 100       %Sets whether fibers and solids can sterically repel each other. 1 is a Boolean that sets steric to
                          %TRUE; 100 is the energy cost of violating sterics
    viscosity = 1         %µm²/s; viscosity of the cytoplasm in an oocyte (Daniels et al., 2006)
    tolerance = 0.01      %Describes the precision of object placement calculations (smaller is more precise)
    kT = 0.0042           %pN.µm; thermal energy of the Brownian system, set for 24C
}
```

%%%%%%%%%%%%%%%%%%%%%%%%%%%%%%%SPACE %%%%%%%%%%%%%%%%%%%%%%%%%%%%%%%%%%%

```
set space cell            %Parameters that describe the simulation space
{
    geometry = ( capsule 5 15 )   %µm; defines the half-lengths of the x and y axes of a capsule object
}
```

%%%%%%%%%%%%%%%%%%%%%%%%%%%%%%%%%FIBERS %%%%%%%%%%%%%%%%%%%%%%%%%%%%%%%%%%%%%

```
set fiber microtubule
{
    rigidity = 20               %pN.µm²; related to persistence length (Gittes et al., 1993)
    segmentation = 0.5          %µm; defines the spacing between calculated points on a fiber
    confine = inside, 100       %Sets confinement of fibers to space; number sets energy cost of violating confinement
    steric = 1, 0.05            %Turns sterics on for this fiber; second number is in µm and defines repulsion radius
    activity = dynamic          %Enables fiber dynamics (growth, shrinkage)
    unit_length = 0.01          %µm; defines minimal length of a "monomer" for fiber growth (must be <= growing_speed
    growing_speed = 0.08        %µm/s; defines growth rate of fiber dynamic end
    shrinking_speed = -0.2      %µm/s; defines shrinking rate of fiber dynamic end
    hydrolysis_rate = 0.8, 2    %s⁻¹; frequency of fiber switching to shrinkage on dynamic end
    rescue_rate = 0.01          %s⁻¹; frequency of fiber switching to growth on dynamic end
    growing_force = 1           %pN; characteristic force for polymer assembly
    binding_key  = 1            %Numeric designator that defines which hands and couples can interact/bind
}

set fiber microtubule2
{
    rigidity = 20               %pN.µm²; related to persistence length (Gittes et al., 1993)
    segmentation = 1            %µm; defines the spacing between calculated points on a fiber
    confine = inside, 100       %Sets confinement of fibers to space; number sets energy cost of violating confinement
    binding_key = 2             %Numeric designator that defines which hands and couples can interact/bind
}
```

%%%%%%%%%%%%%%%%%%%%%%%%%%%%%%%% HANDS %%%%%%%%%%%%%%%%%%%%%%%%%%%%%%%%%%%%%

```
set hand nucleator
{
    unbinding_rate = 0          %s⁻¹; frequency of the hand letting go of a fiber if bound
    unbinding_force = 5         %pN; force descriptor for the Kramer's force-dependent unbinding of the hand
    activity = nucleate         %Sets activity of this hand to generate fibers
    nucleate = 1, microtubule2, ( fiber_length= 0.2 )
    %Defines that this hand will generate a single fiber of type "microtubule2" with an initial length of 0.2 µm.
    display = ( size=2; color= green; )      %Sets display parameters for visualization
}

set hand concrete
{
    binding_rate = 6            %s⁻¹; frequency of the hand binding a nearby fiber
    binding_range = 0.05        %µm; defines minimal distance for hand to be able to bind a fiber
    unbinding_rate = 0          %s⁻¹; frequency of the hand letting go of a fiber if bound
    binding_key = 2             %Numeric designator that defines which hands and couples can interact/bind
```

```
    display = ( size=2; color= purple; )        %Sets display parameters for visualization
}


set hand nucleator2
{
    unbinding_rate = 0                %s⁻¹; frequency of the hand letting go of a fiber if bound
    unbinding_force = 3               %pN; force descriptor for the Kramer's force-dependent unbinding of the hand
    activity = nucleate
    nucleate = 2, microtubule, ( fiber_length= 1.5 )
    %Defines that this hand will generate a single fiber of type "microtubule" with an initial length of 1.5 μm.
    display = ( size=2; color= red; )          %Sets display parameters for visualization
}


set hand cargoD
{
    binding_rate = 2               %s⁻¹; frequency of the hand binding a nearby fiber
    binding_range = 0.1            %μm; defines minimal distance for hand to be able to bind a fiber
    unbinding_rate = 0            %s⁻¹; frequency of the hand letting go of a fiber if bound
    unbinding_force = 6           %pN; force descriptor for the Kramer's force-dependent unbinding of the hand
    binding_key = 2              %Numeric designator that defines which hands and couples can interact/bind
    display = (size=2; color=0xFF000001)        %Sets display parameters for visualization (color is in HEX)
}


set hand dynein
{
    binding_rate = 0.5             %s⁻¹; frequency of the hand binding a nearby fiber
    binding_range = 0.1            %μm; defines minimal distance for hand to be able to bind a fiber
    unbinding_rate = 0.1          %s⁻¹; frequency of the hand letting go of a fiber if bound
    unbinding_force = 8           %pN; force descriptor for the Kramer's force-dependent unbinding of the hand
    binding_key = 1              %Numeric designator that defines which hands and couples can interact/bind
    activity = move             %Sets activity so that this hand can motor on fibers
    max_speed = -0.1           %μm/s; defines maximum translocation (towards the minus end) with no load
    stall_force = 6            %pN; defines force-load at which motor will stall on a fiber
    binding_key = 1           %Numeric designator that defines which hands and couples can interact/bind
    display = (size=2; color=0xFF000001)        %Sets display parameters for visualization (color is in HEX)
}

%%%%%%%%%%%%%%%%%%%%%%%%%%%%%%%%SINGLES %%%%%%%%%%%%%%%%%%%%%%%%%%%%%%%%%

set single spindleNucleator
{
    hand = nucleator2            %Defines the hand on a simple agent
    stiffness = 100             %pN/μm; used to calculate strain and deformation of single under force
}


set single corticalNucleator
{
    hand = nucleator            %Defines the hand on a simple agent
    activity = fixed           %Sets this single to be fixed in space (does not move with Brownian)
    stiffness = 1000          %pN/μm; used to calculate strain and deformation of single under force
}


set single corticalGlue
{
    hand = concrete           %Defines the hand on a simple agent
    confine = surface        %Sets this single to be fixed on the edge of the 2D space
    stiffness = 500         %pN/μm; used to calculate strain and deformation of single under force
}
```

%%%%%%%%%%%%%%%%%%%%%%%%%%%%COUPLES %%%%%%%%%%%%%%%%%%%%%%%%%%%%%

```
set couple Dynein
{
    hand1 = cargoD              %Defines the hand on an agent that can bind two fibers
    hand2 = dynein             %Defines the hand on an agent that can bind two fibers
    stiffness = 100            %pN/µm; used to calculate strain and deformation of couple under force
    fast_diffusion = 1         %Boolean; if enabled unbound couples are not given explicit positions but are presumed
                               %to diffuse so quickly they can interact with a random fiber at any point.
    length = 0.03              %µm; defines the length of the linker between two hands
    activity = crosslink       %Sets couple to bind fibers with both hands and transmit forces between them
}
```

%%%%%%%%%%%%%%%%%%%%%%%%%%%% SOLIDS %%%%%%%%%%%%%%%%%%%%%%%%%%%%%%%

```
set solid spindle
{
    confine = all_inside, 100  %Sets solid to be confined inside the space with an energy cost of 100 for violations
    steric = 1                 %Boolean; spindle solids cannot be crossed by other steric components
    display = { style=6 }      % Sets display parameters for visualization
}

new space cell
```

%%%%%%%%%%%%%%%%%%%%%%%%%%%%%%% RUN %%%%%%%%%%%%%%%%%%%%%%%%%%%%%%%%%

```
new 1 solid spindle            %Generates a solid consisting of many points, some of which are beads and some of
                               %which are nucleators that generate spindle pole microtubules. This code generates one
                               %specific spindle geometry. Several others were also run to compare different spindles.
                               %first three numbers define placement (X,Y,Z) relative to the central coordinates of the
                               %solid at any given timepoint.
{
    nb_points = 34                                      %Sets number of points that make up the solid
    point0 = 0   1.2  0, 0.6                            %Defines a bead of radius 0.6 µm
    point1 = 0   -1.2  0, 0.6                           %Defines a bead of radius 0.6 µm
    point2 = 0.6   0  0, 1.4                            %Defines a bead of radius 1.4 µm
    point3 = -0.6  0  0, 1.4                            %Defines a bead of radius 1.4 µm
    point4 = 1.625 1.06 0  , 0, spindleNucleator        %Defines a nucleator on the spindle pole
    point5 = 1.393 1.174 0  , 0, spindleNucleator       %Defines a nucleator on the spindle pole
    point6 = 1.161 1.289 0  , 0, spindleNucleator       %Defines a nucleator on the spindle pole
    point7 = 0.929 1.403 0  , 0, spindleNucleator       %Defines a nucleator on the spindle pole
    point8 = 0.696 1.517 0  , 0, spindleNucleator       %Defines a nucleator on the spindle pole
    point9 = 0.464 1.631 0  , 0, spindleNucleator       %Defines a nucleator on the spindle pole
    point10 = 0.232 1.746 0  , 0, spindleNucleator      %Defines a nucleator on the spindle pole
    point11 = 0 1.86 0  , 0, spindleNucleator           %Defines a nucleator on the spindle pole
    point12 = -0.232 1.746 0  , 0, spindleNucleator     %Defines a nucleator on the spindle pole
    point13 = -0.464 1.631 0  , 0, spindleNucleator     %Defines a nucleator on the spindle pole
    point14 = -0.696 1.517 0  , 0, spindleNucleator     %Defines a nucleator on the spindle pole
    point15 = -0.929 1.403 0  , 0, spindleNucleator     %Defines a nucleator on the spindle pole
    point16 = -1.161 1.289 0  ,   0, spindleNucleator   %Defines a nucleator on the spindle pole
    point17 = -1.393 1.174 0  , 0, spindleNucleator     %Defines a nucleator on the spindle pole
    point18 = -1.625 1.06 0  , 0, spindleNucleator      %Defines a nucleator on the spindle pole
    %%%%%%%%%%%%%%%%%%%%%%%%%%%%%%%%%%%%%%%%%%%%%%%%%%%%%
    point19 = 1.625 -1.06 0  , 0, spindleNucleator      %Defines a nucleator on the spindle pole
    point20 = 1.393 -1.174 0  , 0, spindleNucleator     %Defines a nucleator on the spindle pole
    point21 = 1.161 -1.289 0  , 0, spindleNucleator     %Defines a nucleator on the spindle pole
    point22 = 0.929 -1.403 0  , 0, spindleNucleator     %Defines a nucleator on the spindle pole
    point23 = 0.696 -1.517 0  , 0, spindleNucleator     %Defines a nucleator on the spindle pole
    point24 = 0.464 -1.631 0  , 0, spindleNucleator     %Defines a nucleator on the spindle pole
    point25 = 0.232 -1.746 0  , 0, spindleNucleator     %Defines a nucleator on the spindle pole
    point26 = 0 -1.86 0  , 0, spindleNucleator          %Defines a nucleator on the spindle pole
    point27 = -0.232 -1.746 0   , 0, spindleNucleator   %Defines a nucleator on the spindle pole
```

```
point28 = -0.464 -1.631 0  , 0, spindleNucleator     %Defines a nucleator on the spindle pole
point29 = -0.696 -1.517 0  , 0, spindleNucleator     %Defines a nucleator on the spindle pole
point30 = -0.929 -1.403 0  , 0, spindleNucleator     %Defines a nucleator on the spindle pole
point31 = -1.161 -1.289 0  , 0, spindleNucleator     %Defines a nucleator on the spindle pole
point32 = -1.393 -1.174 0  , 0, spindleNucleator     %Defines a nucleator on the spindle pole
point33 = -1.625 -1.06 0  , 0, spindleNucleator      %Defines a nucleator on the spindle pole

    position = 16.8 0 0 at 0 0                        %Places the solid in absolute space
    orientation = 1 0 0                               %Aligns the spindle solid to the X axis
}

new 2000 couple Dynein                                %Places 2000 couples randomly in the space
new 100 single corticalGlue                           %Places 100 singles
{
    position = rectangle 2 4 at 16.5 0                %Places these singles in a rectangle centered at 16.5 in X
}

new 140 single corticalNucleator                      %Places 140 singles
{
    position = arc 30 2.0 at 19.96 0                  Places them in an arc at 19.96 in X with radius 30 and width 2
}

run simul *                                           %Run the simulation
{
    nb_steps = 3000                                   %Number of calculated timepoints
    nb_frames = 3                                     %Number of frames generated for visualization
}

change single corticalNucleator {activity = fixed;}   %Changes single so that they cannot move anymore

run simul *                                           %Run the simulation
{
    nb_steps = 300000                                 %Number of calculated timepoints
    nb_frames = 300                                   %Number of frames generated for visualization
}
```
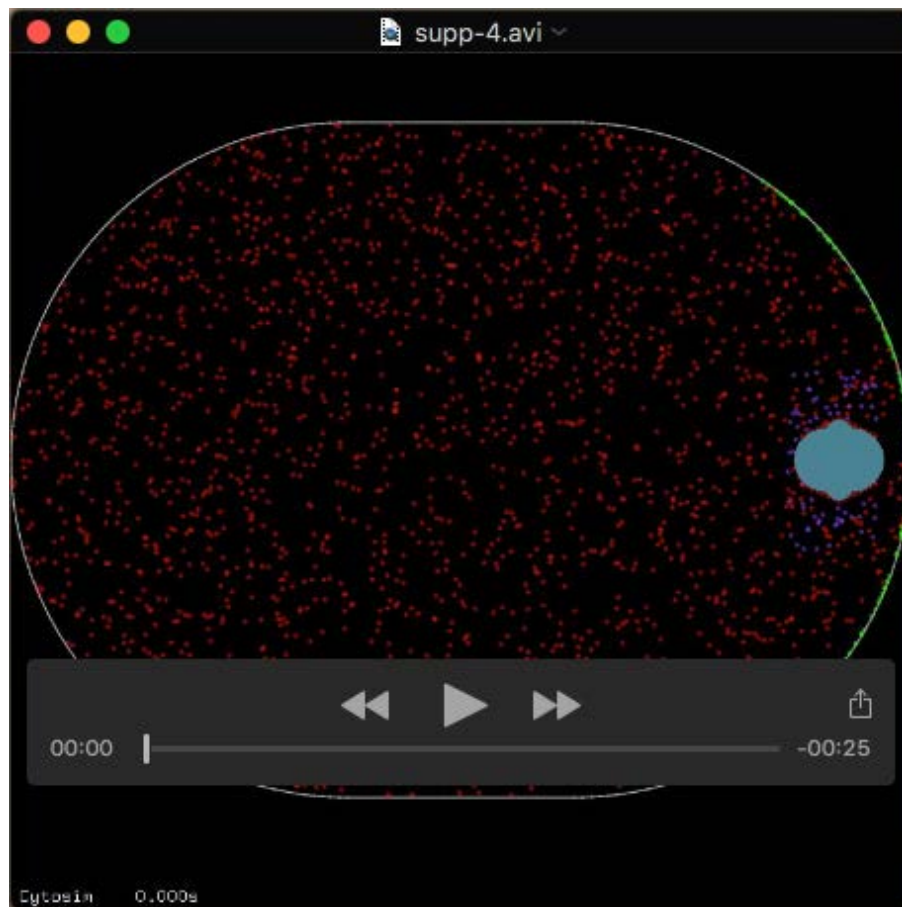
Movies

For all movies: Red dots represent cytoplasmic dynein molecules that associate randomly with astral or cortical microtubules, motor to the minus end, and dissociate with a rate constant that increases with applied force. Pulling toward the cortex occurs transiently when a dynein contacts both a cortical microtubule and an astral microtubule. After the first frame, only dynein molecules engaged with a microtubule are displayed. Astral microtubules emanate from nucleators arranged to mimic the localization of dynein/LIN-5 on control (flat) or *mei-2(ct98)* (pointed) poles. Green dots represent nucleation sites for short cortical microtubules. Purple dots represent a "cortical glue" that resists detachment once close contact between the pole and cortex is achieved. All spindles start at a fixed distance from the cortex and perfectly parallel to the cortex.
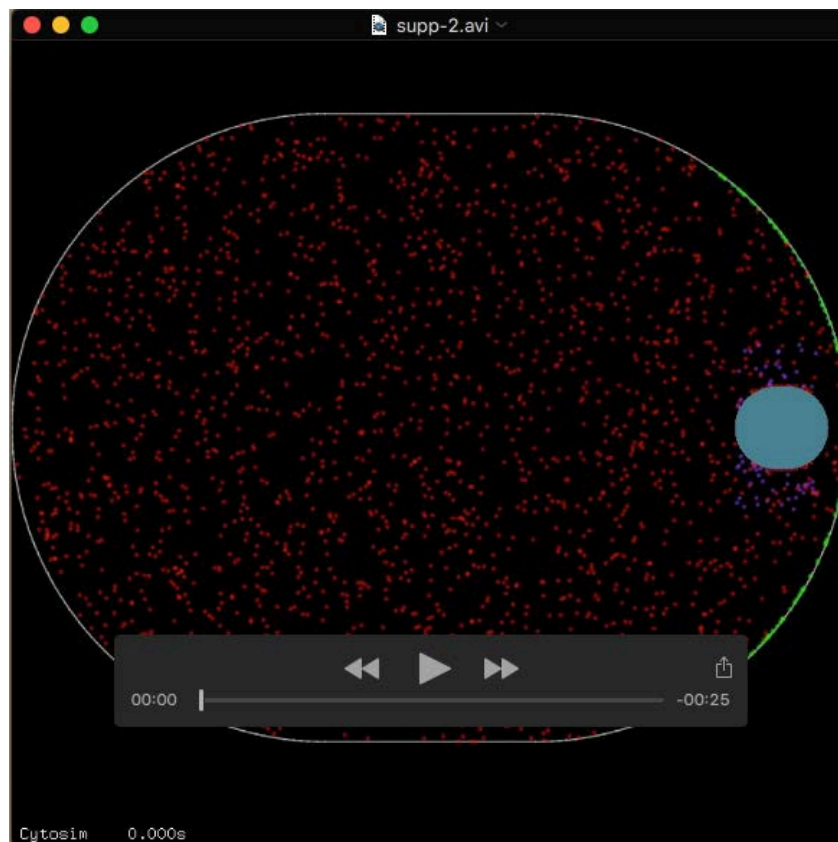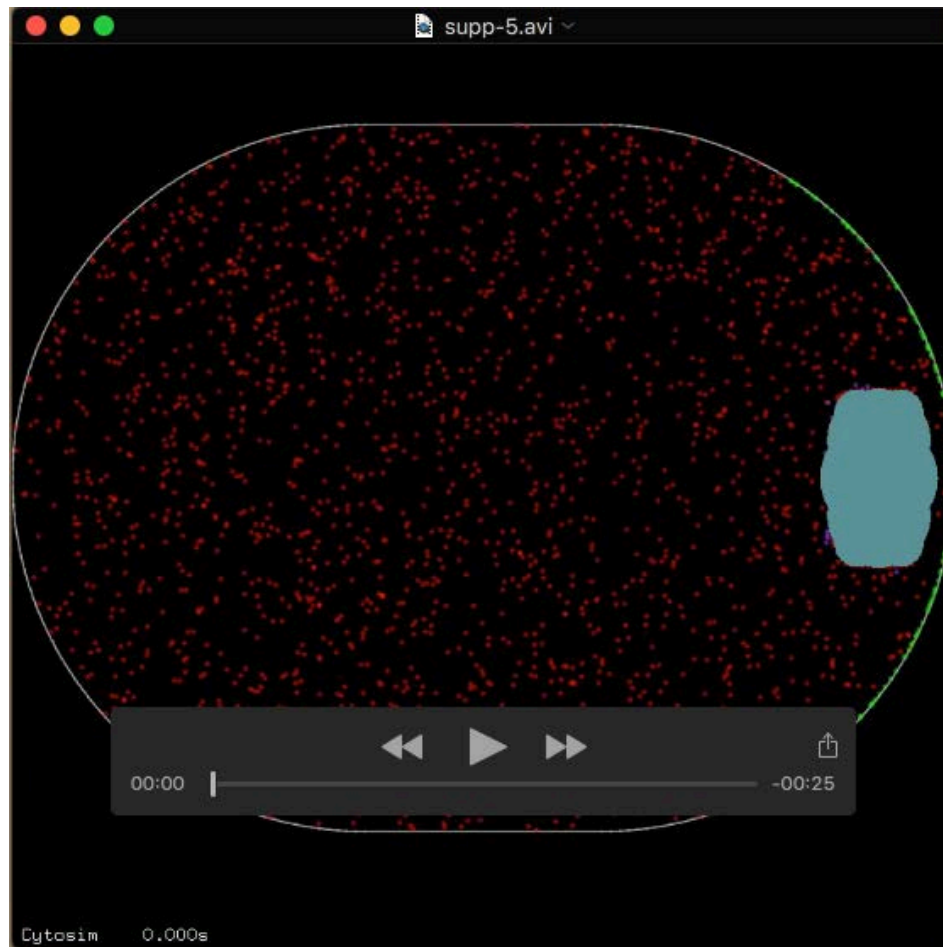

Movie 1. <u>Simulation of rotation of a short (0.9 axial ratio) spindle with flattened poles and short astral microtubules</u>. This shape mimics control spindles midway through rotation. Astral microtubules are short due to a polymerization rate of 0.06 μm/s.
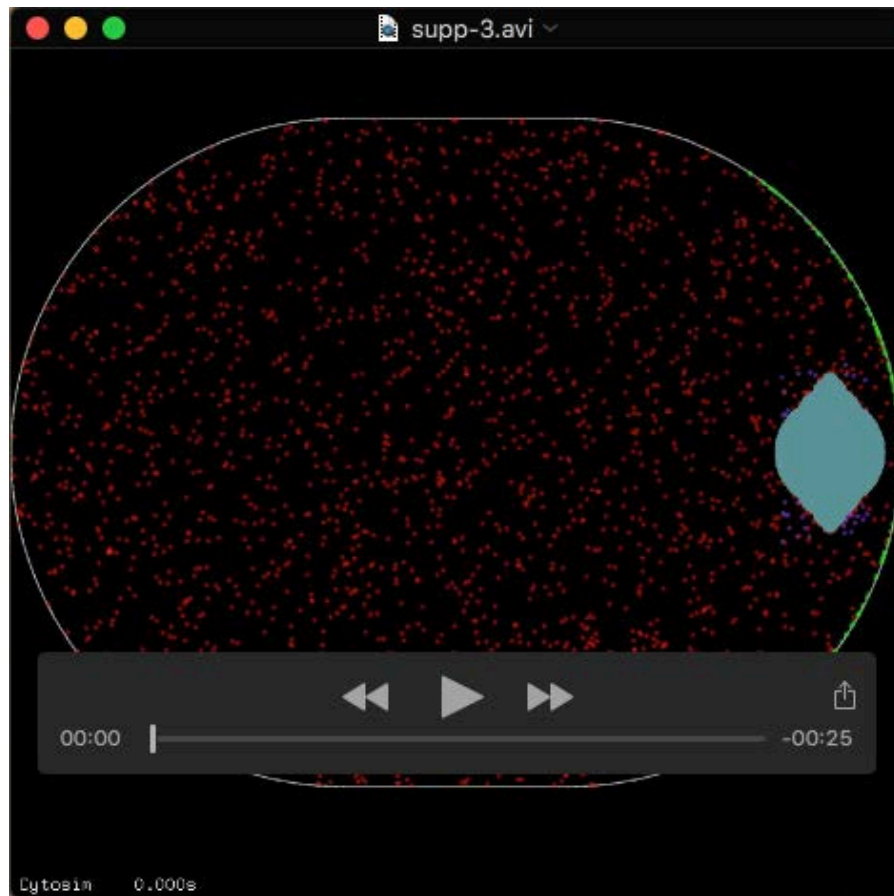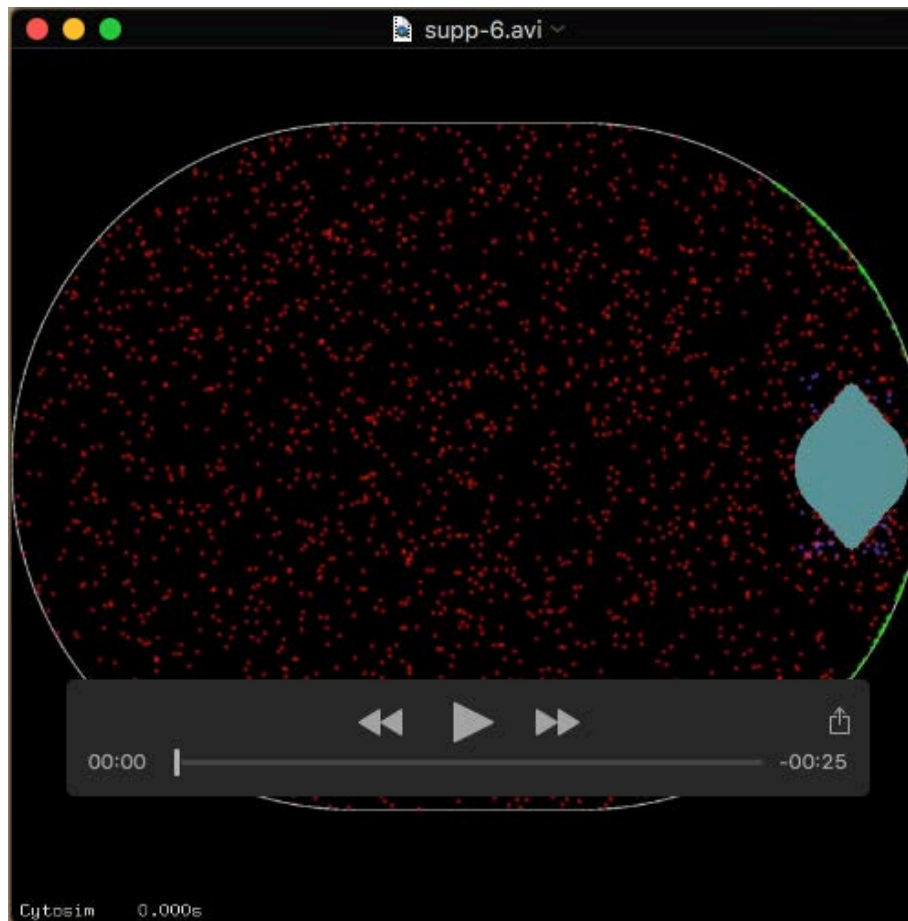
Movie 2. Simulation of rotation of a long (1.5 axial ratio) spindle with pointed poles and short astral microtubules. This shape mimics the shape of the shortest mei-2(ct98) spindles that rotate partially to a diagonal angle relative to the cortex. Astral microtubules are short due to a polymerization rate of 0.06 μm/s.
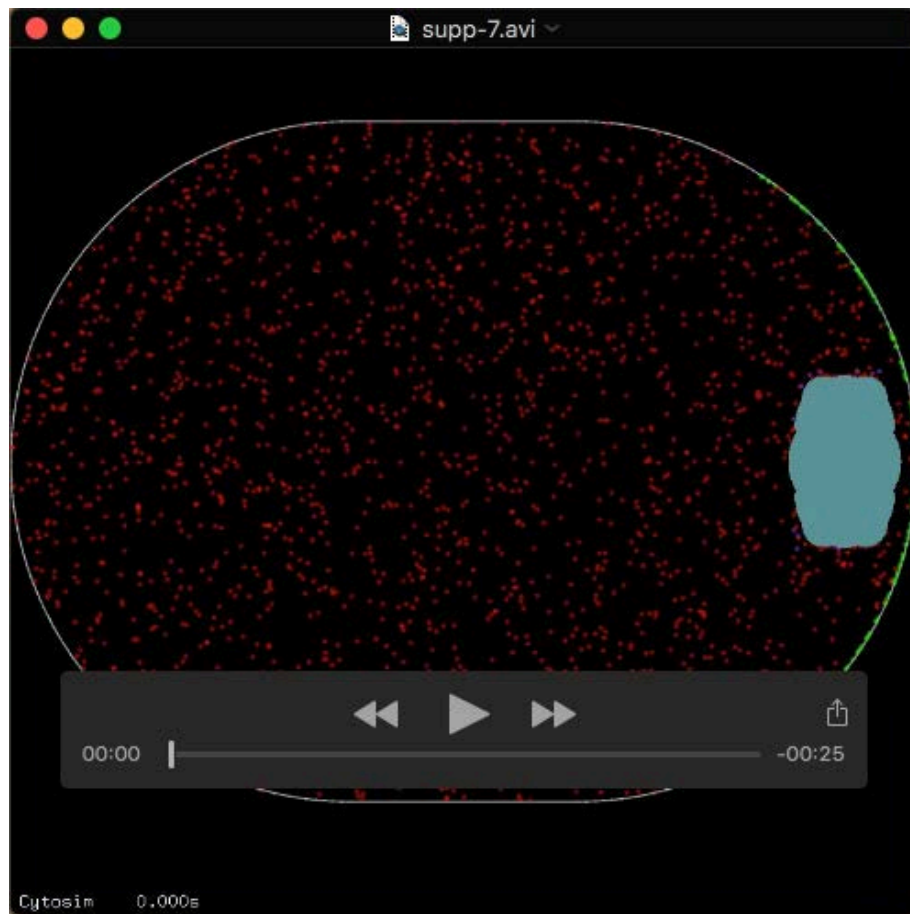
Movie 3. Simulation of rotation of a short (0.9 axial ratio) spindle with pointed poles and short astral microtubules. This spindle has the axial ratio of a control spindle and pointed poles like a *mei-2(ct98)* spindle. Astral microtubules are short due to a polymerization rate of 0.06 μm/s.
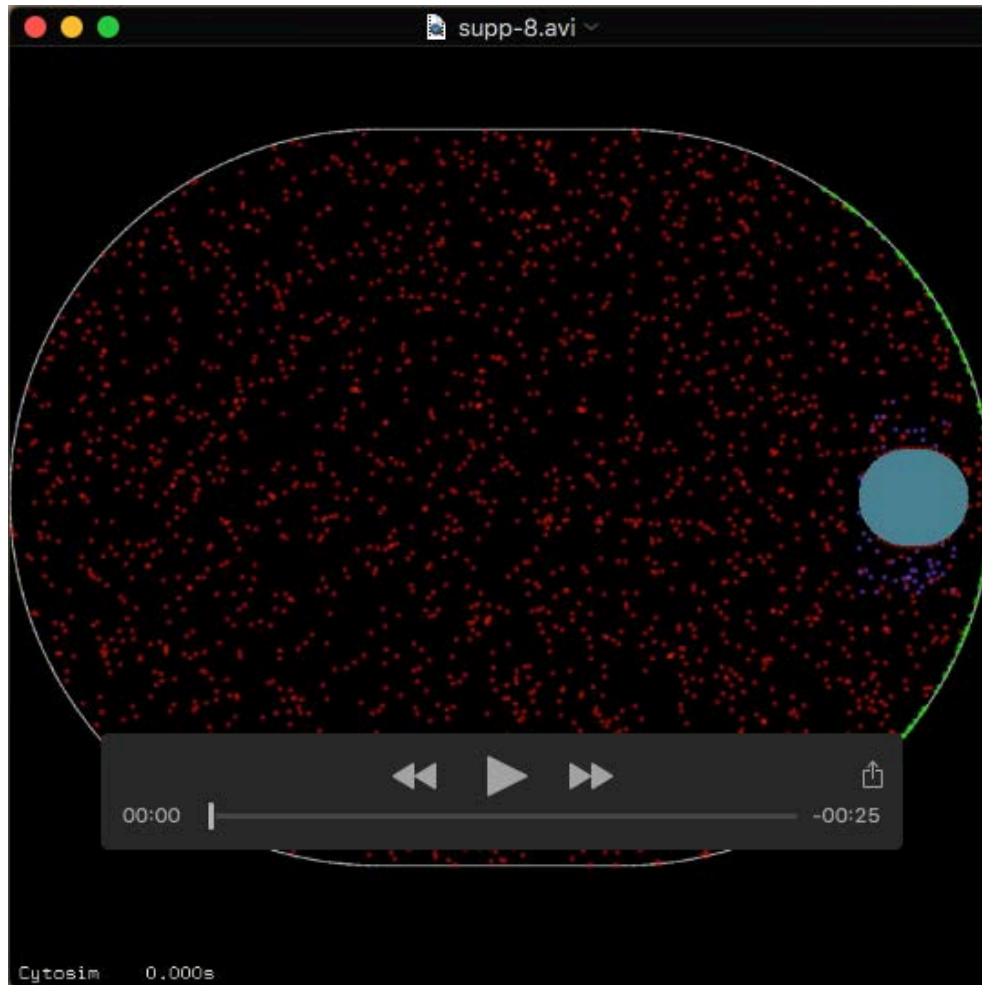
Movie 4. Simulation of rotation of a long (1.5 axial ratio) spindle with flattened poles and short astral microtubules. This spindle has the axial ratio of the shortest *mei-2(ct98)* spindles that rotate partially to a diagonal angle relative to the cortex but with poles shaped like those of a control spindle. This shape is also similar to that of *knl-1,3(kd)* spindles that partially rotate or fail to rotate. Astral microtubules are short due to a polymerization rate of 0.06 μm/s.
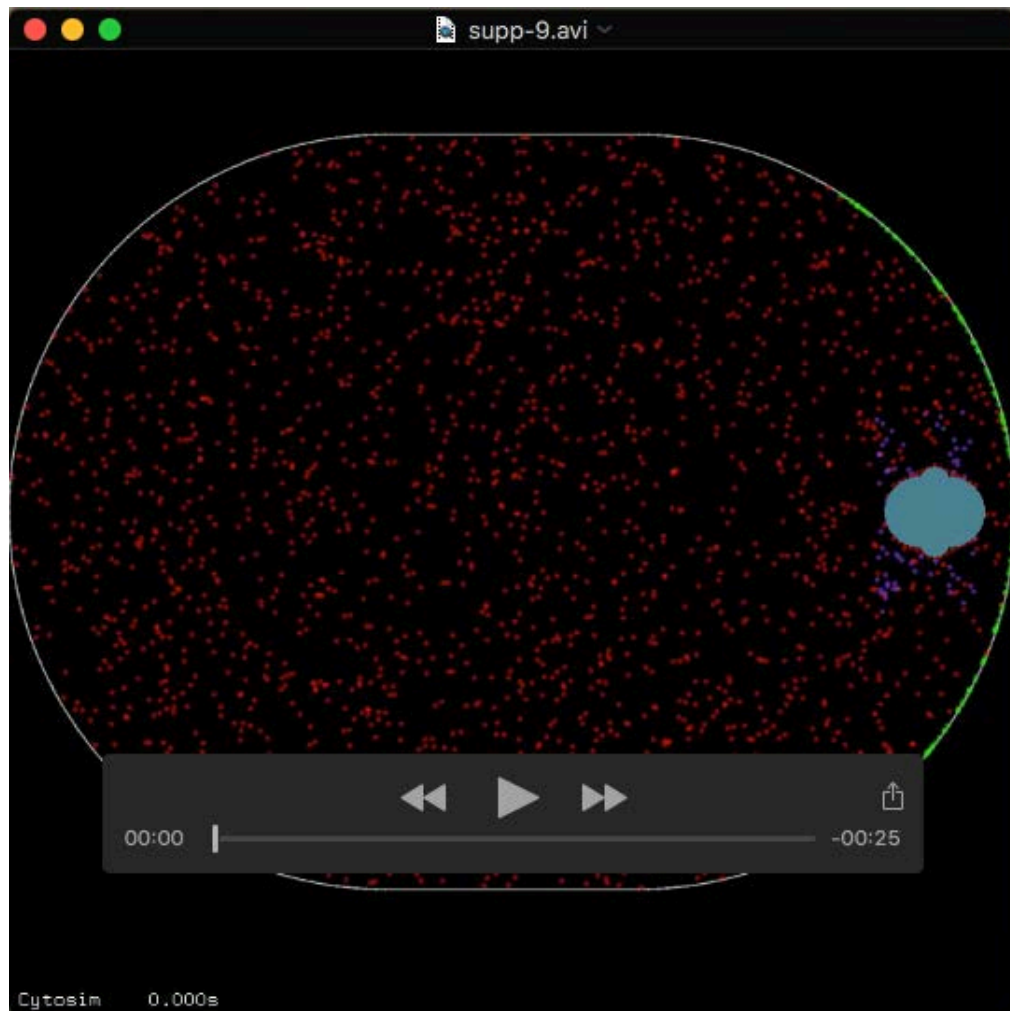
Movie 5. Simulation of rotation of a long (1.5 axial ratio) spindle with pointed poles and long astral microtubules. This shape mimics the shape of the shortest *mei-2(ct98)* spindles that rotate partially to a diagonal angle relative to the cortex. Astral microtubules are long due to a polymerization rate of 0.18 μm/s.

Movie 6. Simulation of rotation of a long (1.5 axial ratio) spindle with flattened poles and long astral microtubules. This spindle has the axial ratio of the shortest *mei-2(ct98)* spindles that rotate partially to a diagonal angle relative to the cortex but with poles shaped like those of a control spindle. This shape is also similar to that of *knl-1,3(kd)* spindles that partially rotate or fail to rotate. Astral microtubules are long due to a polymerization rate of 0.18 μm/s.

Movie 7. Simulation of rotation of a short (0.9 axial ratio) spindle with flattened poles and long astral microtubules. This shape mimics control spindles midway through rotation. Astral microtubules are long due to a polymerization rate of 0.18 μm/s.

Movie 8. Simulation of rotation of a short (0.9 axial ratio) spindle with pointed poles and long astral microtubules. This spindle has the axial ratio of a control spindle and pointed poles like a *mei-2(ct98)* spindle. Astral microtubules are long due to a polymerization rate of 0.18 μm/s.